An Analysis of the Radiation Damage to the ATLAS Semiconductor Tracker End-Caps

Declan Andrew Millar

University of Southampton
Highfield
Southampton
SO17 1BJ
United Kingdom

A thesis submitted to the
School of Physics and Astronomy
in partial fulfilment of the requirements for

Master of Physics
Particle Physics with a Research Year Abroad at CERN

May 2013

Abstract

The motivation, theoretical principles and analytical procedure for an assessment of the radiation damage to the ATLAS SCT end-caps is presented. An analysis of the leakage current across end-cap modules is performed for 2011 and 2012 data. A comparison between the observed and expected leakage current is made, with measurements favouring the shape of the theoretical evolution. Measured data is found to be systematically lower than predicted for a large subset of end-cap modules, while the remainder show surface current effects which interfere with bulk current observation. Uniform differences for modules at different radial distances suggest a radial temperature distribution in the end-caps, with absolute silicon sensor temperature to be established in further analysis.

Acknowledgements

Principally, I would like to thank my supervisor Steve McMahon for his excellent guidance and help, as well as his valuable time, patience and eagle eyes. My gratitude goes too to Saverio D'Auria for welcoming me in to his office. A special mention goes also to my predecessor Jack Roberts.

Many thanks to the University of Southampton and the Science and Technology Facilities Council for this fantastic opportunity. Particular gratitude goes to Stefano Moretti for organising the placement.

Special thanks go to my flatmates Ben and Rhys for putting up with me all year, in addition to the other Southampton students Alex, Chris and Nicole. Without the combined effort of Alex, Ben and Rhys, I'd never have figured out how to open a computer terminal. I'm also grateful to all the UK LTA students for being so friendly and welcoming.

Contents

Chapter 1

Introduction

1.1 Background

The Semiconductor Tracker (SCT) is a component of the ATLAS Inner Detector (ID) at the Large Hadron Collider (LHC) at CERN. The second detector subsystem from the interaction point, it is a silicon micro-strip detector designed to track the paths of charged particles in the intermediate radial range of the ID. Its close proximity to innumerable high energy collisions means that the SCT operates in an extremely intense radiation field, where radiation damage to the silicon material instigates deterioration of its detector properties.

An effect of radiation damage is an increase in the leakage current I_{leak} of the SCT modules. This current equates to background noise across the module sensors, which interferes with the current induced by high energy charged particles. Critical increases in the leakage current of SCT modules can be catastrophic by triggering thermal runaway. This arises due to a positive feedback loop between increases in current and temperature. The high resulting current makes resolving the paths of traversing particles impossible. It is important, therefore, to keep leakage current and module temperature within safe limits. Direct measurement of leakage current evolution is convenient for determining the radiation damage in the silicon bulk, which affects other sensor properties, such as the depletion voltage.

The maximum permissible magnitude of leakage current before thermal runaway is 5 mA [1]. SCT modules are designed to account for irradiation, with a proposed lifetime based on previous experience and a theoretical understanding. Long term predictions propose an end-of-life SCT I_{leak} of around $2 - 3$ mA [2], thereby granting an error factor of about 2.

1.2 Motivation

In 2010 an analysis of the SCT leakage current was conducted [2]. This was done by comparing the measured leakage current data I_{data} with a theoretical current evolution I_{HM}, calculated using the Harper model (HM). Figure 1.1 shows that at small radial distances from the beamline, the ratio of measured to expected leakage current $R_{leak} = I_{data} / I_{HM}$ was as high as around 2. The findings were a concern as they suggested that, if this discrepancy persists, I_{leak} will be

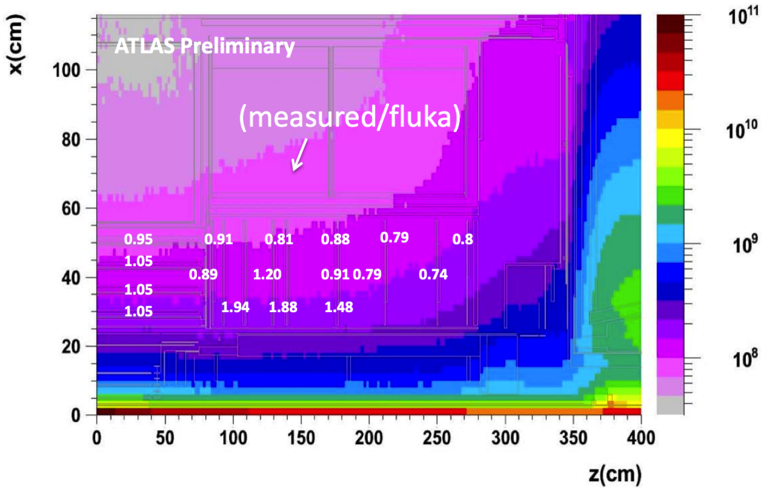

Figure 1.1: A plot from the 2010 analysis displaying R_{leak} for different regions of the SCT. The FLUKA Monte Carlo 1 MeV neutron equivalent fluence 10^{11} $\mathrm{MeVn_{eq}cm^{-2}fb^{-1}}$, with axis on the right, is reported via a heat map. This image shows a top-down view of the detector, with the barrel on the left, at small z, and end-cap A on the right. [2]

twice as high as expected at end-of-life. This would, effectively, reduce the margin for error to zero.

A more concerning possibility is that the discrepancy found in 2010 could increase over subsequent years, resulting in a runaway current before the ATLAS experiment reaches the end of its functional lifetime. The comparisons also indicate that the barrel modules show much more consistent agreement with the theoretical evolution.

This consistency has been subsequently demonstrated by Taka Kondo of KEK. The concurrent study shows that current measurements repeatedly conform to predictions over 2010, 2011 and 2012. Figure 1.2 shows a sample of obtained results with 2011 data. It is evident from the shape of the distribution that I_{data} follows the HM evolution, though with a uniform relative magnitude R_{leak} of about 0.9, within the uncertainty of the model.

These analyses suggest that there are important differences for the end-cap modules. This motivates an additional study, with more recent data, in order to investigate this disparity more closely. If radiation damage is found to be increasing at an unforeseen rate, it suggests that these devices will not survive the envisaged operational duration of the ATLAS experiment.

1.3 Aims

The aim of this analysis is to observe the evolution of leakage current across SCT end-cap modules in 2011 and 2012, in order to determine whether it is in keeping with what is expected from theoretical predictions.

The Harper model is used to predict the evolution of leakage current for each region of the end-cap that receives a uniform irradiation. Absolute measurements of leakage current are then extracted on a certain date for every end-cap module. These are then averaged over each of

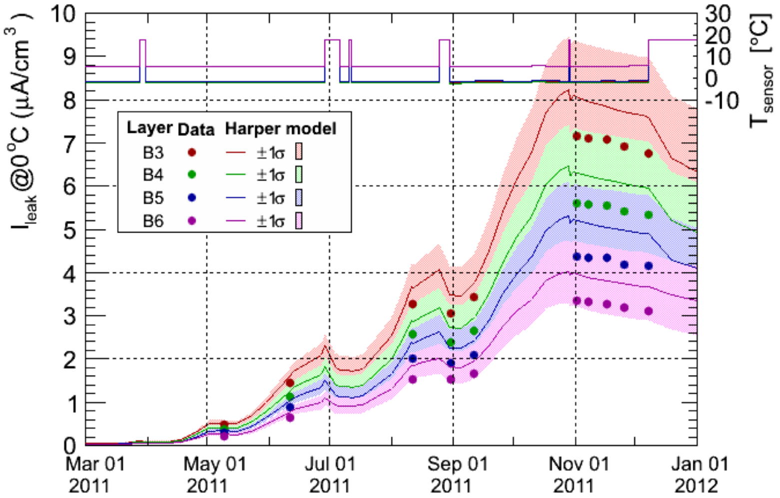

Figure 1.2: The results of a 2011 comparison showing I_{data} (points) against the current evolution expected from the Harper model I_{HM} (lines) with I_{HM} uncertainty reported by coloured bands. [3]

the corresponding regions and compared to the expected magnitude by taking the ratio $R_{leak} = I_{data}/I_{HM}$. Such comparisons are made throughout 2011 and 2012 in order to observe any trends over time.

Additionally, in order to confirm that the analytical method is appropriate, a 2011 cross-check of the barrel modules is also performed, and the results compared in juxtaposition with the parallel analysis.

In this thesis, firstly, the design of the LHC and ATLAS detector is outlined in chapters 2 and 3, respectively. Following this, chapter 4 provides an overview of the physics behind semiconductors and why their properties make them effective as particle detectors. Details on the specific parameters of the SCT are given in chapter 5. The mechanisms responsible for radiation damage, as well as the Harper model, are described in chapter 6. Subsequently, chapter 7 details the specific SCT parameters used in generating these predictions, along with the results. Chapter 8 explains how current measurements are processed in order to extract observations for a certain time and detector module. A comparison of predictions and measurements is made in chapter 9, with the conclusions in chapter 10.

Chapter 2

The LHC: Large Hadron Collider

The Large Hadron Collider (LHC) is currently the highest energy particle accelerator ever constructed. Principally a proton-proton pp collider, the designed centre-of-mass energy for these collisions is 14 TeV, with a luminosity of $10^{34}\,\mathrm{cm}^{-2}\,\mathrm{s}^{-1}$ [5]. During running in 2010 and 2011 the pp energy was 7 TeV, which increased to 8 TeV in 2012. It can also collide lead ions with an energy of 2.8 TeV per nucleon and a peak luminosity of $10^{27}\,\mathrm{cm}^{-2}\,\mathrm{s}^{-1}$. The high energy and luminosity provided by the LHC enables the observation of rare interactions in order to identify new physics processes, allowing the analysis of previously untested theories.

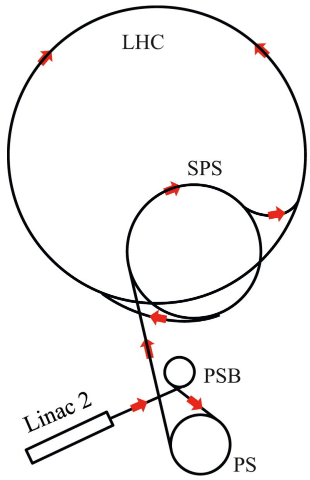

Figure 2.1: Schematic of the LHC proton injector chain. [4]

Proton beams in the LHC are accelerated in pulses, distributing the particles in to 'bunches' consisting of approximately 10^{11} protons. Each beam comprises 2808 bunches, which are nominally separated by 25 ns, though, currently, 50 ns bunch spacings are common.

The accelerator chain begins with the linear accelerator (Linac 2). A subsequent booster (PSB) injects particles into the Proton Synchrotron (PS), which accelerates them up to 26 GeV. Upon reaching this energy, the protons are inserted into the Super Proton Synchrotron (SPS) which increases their energy to 450 GeV.

The particles are then injected in to the LHC, which is installed in a tunnel with a circumference of 27 km. Around the ring, there are eight straight sections, each followed by a portion which bends the particles using magnetic fields. A single straight section contains the microwave cavities that accelerate the protons to their collision energy. Another section contains the beam dump, which removes the beams when their luminosity has dropped below useful limits. Two sections use magnetic fields to focus the beams, reducing their cross-sectional area.

The remaining four straight sections can cross them, resulting in an interaction point. When running with stable beams bunch crossings occur with a frequency of 40 MHz, each generating around twenty pp collisions. Installed on these sections are the detectors that reconstruct the resultant interactions. The largest collaborations are ATLAS, CMS (Compact Muon Solenoid), LHCb (LHC beauty) and ALICE (A Large Ion Collider Experiment) [6].

Chapter 3

ATLAS: A Toroidal LHC Apparatus

3.1 Physics Goals

The Standard Model (SM) of Particle Physics ties together three seemingly disparate interactions: electromagnetism EM, the weak force and the strong force. In doing so it describes all known elementary particles and their interactions[1]. It is underpinned by relativistic quantum field theory, with every fundamental particle an excitation of an underlying field. All particles can be split in to two categories, fermions and bosons. The former spin-$\frac{1}{2}$ particles compose all visible matter and can be further sub-categorised in to leptons and quarks. These are each divided in to three generations of increasing mass.

Particle	Flavour			$Q/\lvert e\rvert$
leptons	ν_e	ν_μ	ν_τ	0
	e	μ	τ	-1
quarks	u	c	t	$+\frac{2}{3}$
	d	s	b	$-\frac{1}{3}$

Table 3.1: The Standard Model Fermions

The SM interactions are mediated by spin-1 vector bosons, quanta of gauge fields. Photons γ mediate EM between all charged particles. The weak force, interacting between all fermions, is carried by the $W\pm$ and Z_0 bosons. Strong interactions are mediated by gluons, which couple to colour charge. This is distinct from charge and has a 3-way multiplicity of red, green and blue. Quarks, the sole fermions with colour charge, are never observed in isolation, always confined in composite particles known as hadrons. Two such hadrons are the proton and neutron, respectively, composed of uud and udd.

In the SM, all elementary particles acquire mass via the Higgs mechanism. The Higgs field has a non-zero vacuum expectation value and its introduction leads to a spontaneous breaking of the electroweak gauge symmetry. The resulting massless degrees of freedom, the Goldstone

[1]This section briefly outlines the standard model and the underpinning field theories. A more thorough description may be found in [7, 8].

Bosons, are 'eaten' by the gauge fields to give masses to the 3 vector bosons of the weak interaction. Fermions acquire their mass via a Yukawa interaction with the Higgs field. An excitation in this field is a spin-0 scalar particle, the Higgs Boson.

The Higgs, however, prior to the running of the LHC, was undiscovered, the last missing ingredient of the SM. Finding evidence of this particle was the principle goal of the ATLAS collaboration. In March 2013, from combined signal analysis, the mass of a newly discovered boson was given as approximately 125.5 GeV [9]. A subsequent spin analysis in April found that data strongly favoured this boson to have spin-0 [10]. With these findings, it was decided that, beyond reasonable doubt, the newly discovered particle is the Higgs boson.

Finding the Higgs is significant, as the mechanism by which all fundamental particles are given mass has now been established. However, the SM appears to be an incomplete description. So far, for example, there is no account of the neutrino ν masses, nor an explanation for the apparent matter/antimatter asymmetry in the universe. Many models, such as super-symmetry, have been proposed that attempt to explain these phenomena. Continuing analysis of the properties of this new particle is imperative in determining whether it fits in to the SM, or belongs to theories beyond the standard model [11].

3.2 Coordinate system

The coordinate system and nomenclature used to describe the ATLAS detector is outlined briefly here, since it will be referred to repeatedly. The ATLAS detector is located at 'point one' of the LHC ring, with the nominal interaction point defined as the origin of the ATLAS coordinate system. The z-axis is defined by the beam axis, with the x-y plane perpendicular to beam direction. The positive x-direction points towards the centre of the LHC ring, with the y-direction pointing directly upwards. The A side of ATLAS is defined to be that with positive z, while the C side has negative z.

Due to the symmetry of ATLAS, it is also common to use cylindrical co-ordinates (r, ϕ, z). The transverse radial distance from the beam pipe r is given by $r = \sqrt{x^2 + y^2}$, while the azimuthal angle ϕ is measured from the positive x-axis. Additionally, the polar angle θ is the angle from the positive z-axis [12].

For describing tracks of the high energy particles it useful to define the rapidity, y [6]:

$$y = \frac{1}{2} ln \frac{E + p_L}{E - p_L} \tag{3.1}$$

This is because differences in the y coordinate between two events[2] are invariant under longitudinal Lorentz boosts (in the z-direction). This is desirable, as the colliding partons[3] have unknown original longitudinal momentum p_L. In the ultra-relativistic (massless) limit, where we assume all particles are travelling at the speed of light, this quantity can be closely approximated by pseudorapidity η:

[2]Here, 'event' reports the more general spacetime coordinate, rather than, say, a bunch crossing, as it typically refers to at the LHC and throughout this thesis. Though, of course, it may report both.

[3]A parton refers to the constituent gluons and quarks within hadrons, in this case within protons.

$$\eta = \frac{1}{2} ln \frac{|\mathbf{P}| + p_L}{|\mathbf{P}| - p_L} = -ln \left(tan \left(\frac{\theta}{2} \right) \right) \tag{3.2}$$

Note that, unlike rapidity, pseudorapidity depends only on the angle between the beam line and the particle momentum **P**, and not on the energy of the particle E. This parameter is convenient for describing the coverage of the detector. The 'forward' sections of ATLAS refer to regions of the detector that are at high pseudorapidity.

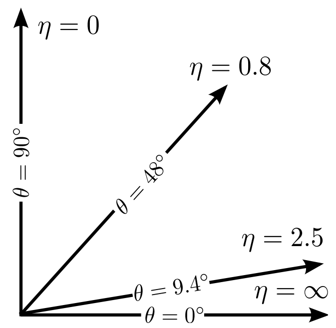

Figure 3.1: As ϕ goes to 0, η approaches infinity.

3.3 Detector Anatomy

ATLAS, along with CMS, is one of two general purpose detectors on the LHC designed to track and identify the particles resulting from proton-proton collisions. The resulting high particle energies and multiplicities, interaction rates and need for precision measurements necessitate that ATLAS sets new standards in particle detection [12].

One important standard is hermeticity, which accounts for the capacity of a particle detector to observe all possible decay products of an interaction between subatomic particles in a collider. A hermetic detector incorporates maximum coverage around the interaction and accounts for all particle multiplicities with various types of sub-detectors. In order to accurately recreate high energy physics events it is important to maximise the hermeticity of the detector as it allows for measurements of missing momentum. This is necessary identifying for particles that interact very weakly with matter, where a direct detection is virtually impossible, such as neutrinos.

The ATLAS detector has a symmetrical, cylindrical form 44 metres long, 25 metres in diameter and weighing 7000 tonnes, composing multiple subsystems. These components can be approximately separated in to four categories: the inner detector, calorimeter systems, muon detector and magnet systems. The first three compose the main detector sub-systems of ATLAS. Moving radially outward from the interaction point, the first is the inner detector, a tracker, which allows for measurement of momentum for charged particles as they curve in a magnetic field. Next there are calorimeters, which determine the energy of most charged and neutral particles via their direct absorption. Lastly comes the muon system, which measures the momentum of the principle detectable particles not halted by calorimeters.

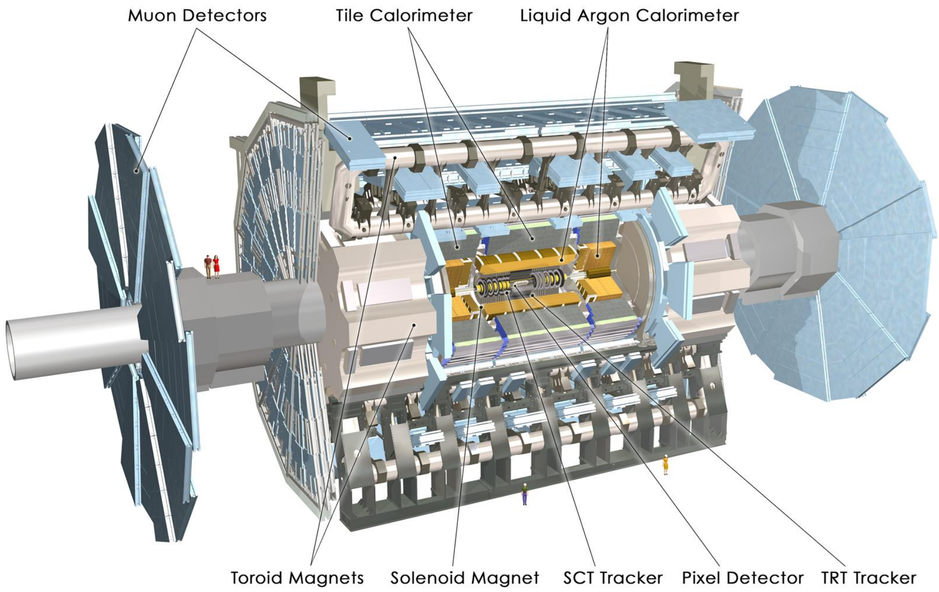

Figure 3.2: A schematic of the full ATLAS apparatus, labelling principle detector components. A sense of scale may be inferred from those people drawn on the shielding and floor. [13]

Each particle has a unique combination of signals in each detector sub-system, allowing different particles to be identified. The distinct information from these interactions together allow the accurate tracking of all particles, and a reconstruction of each event. Figure 3.2 shows a cutaway diagram, labelling the principle components of the detector. Each sub-system composes a central barrel region which is responsible for particle tracking in the small η region and two end-caps on each the A and C side which cover the high η forward regions. The total pseudorapidity coverage of the ATLAS detector extends from $|\eta| = 0$ to $|\eta| = 4.9$ [12].

3.3.1 Magnet Systems

ATLAS requires two independent magnet systems. The first is a central solenoid surrounding the inner detector, providing a field strength of 2 Tesla. Situated before the calorimeter systems, it is designed to be as thin as possible, in order to minimise the energy loss of a particle prior to reaching the surrounding subsystems.

The second, toroidal, magnetic system encloses the muon-spectrometer and consists of eight large coils in the barrel region accompanied by 8 smaller coils in each of the end-caps, providing respective field strengths of 1T and 0.5T.

The super-conducting magnets are cooled to temperatures of 4 Kelvin using a system of liquid helium cryogenics. Both magnet systems have a similar purpose: they bend the paths of charged particles traversing the encompassing sub-systems in order to resolve their momenta.

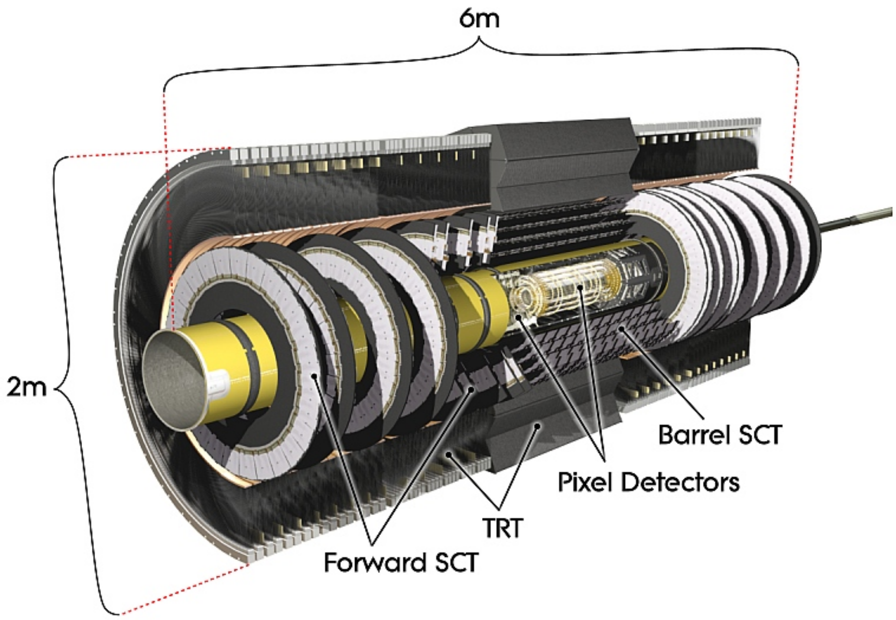

Figure 3.3: A cutaway schematic of the ATLAS Inner Detector, labelling principle sub-systems. [14]

3.3.2 Inner Detector

The inner detector (ID) is the central detector subsystem, situated closest to the origin. It has an η coverage of ± 2.5. The principle purpose of the ID is the precise measurement of position and momentum for charged particles. This information is critical in determining the primary vertex positions and impact parameters of interactions.

For every bunch crossing a large number of particles with high multiplicity emerge within $|\eta| < 2.5$, creating an extremely high track density in the detector [12]. To achieve the required momentum and vertex resolutions for isolating frontier physics processes, a fine detector granularity is required. The ID sub-systems provide this function. Moving radially outward from the interaction point these are the Pixel detector, the Semiconductor Tracker (SCT) and the Transition Radiation Tracker (TRT).

The Pixel detector is a semiconductor detector. Sensors are embedded with 2D arrays of small, rectangular p-type silicon, or 'pixels'. There are 80 million of these pixels in total. With a pitch (section 5.3) of $50\,\mu\text{m} \times 400\,\mu\text{m}$ they provide a resolution of $14\,\mu\text{m}$ in $r\phi$ and $87\,\mu\text{m}$ in z. Their high granularity makes them ideal for distinguishing tracks at high particle flux density. This data allows accurate 3D vertex reconstruction for charged tracks and the determination of the transverse impact parameter to $<15\,\mu\text{m}$.

The SCT operates similarly to the Pixel, yet features silicon strips. The SCT is the principle focus of this thesis and is described in greater detail in chapter 5, while the general principles behind all semiconductor detectors are detailed in chapter 4.

At the outermost radii, the TRT provides a large number of additional lower-resolution tracking measurements, as well as some particle identification. It consists of gas filled 'straws' embedded in dense radiator material. Ultra-relativistic particles emit transition radiation when crossing the interface of two media with different dielectric constants [15]. The frequency of this radiation is dependent on the Lorentz factor:

$$\gamma = \frac{1}{\sqrt{1 - \frac{v^2}{c^2}}} = \frac{E}{mc^2} \tag{3.3}$$

This factor is different for particles of the same momentum, but different mass, allowing the TRT to distinguish between electrons and other particles, such as pions[4].

3.3.3 Calorimeters

The calorimetry system aims to stop and directly measure the energy of neutral and charged particles, such as electrons e^-, photons γ and jets[5]. This consists of alternating layers of dense absorbing and scintillating material, followed by photo-detectors. The intensity of the light is then used to determine the energy of the particles.

The calorimetry system composes an electromagnetic calorimeter surrounded by a hadronic calorimeter. Low mass electromagnetically interacting particles such as e^- and γ are absorbed by the first calorimeter, while hadronic matter penetrates further. Only neutrinos and high energy muons may escape through the calorimeter system. Particle showering is an important process for this procedure and is described in more detail in section 7.2.1.

3.3.4 Muon Detector

Muons μ are the sole detectable particles able to traverse both the inner detector and calorimeters. The muon spectrometer, along with the accompanying toroidal magnets, dominate the outward appearance of the ATLAS detector. The system consists of thousands of charged particle sensors, similar in design to the straws of the TRT, yet with larger diameters. By altering the paths of muons and tracking the resultant motion their momentum is determined with high precision.

[4] Pi-mesons (π^+, π^-, π^0) are the lightest of mesons, which consist of one quark and one anti-quark. π^+ (π^-) consists of $u\bar{d}$ ($d\bar{u}$), while π^0 exists as the superposition state $\frac{1}{2}\left(u\bar{u} - d\bar{d}\right)$.

[5] Jets are narrow cones of particles produced by the hadronisation of a parton due to colour confinement.

Chapter 4

Principles of Semiconductor Detectors

4.1 Band Theory

Electrons bound to isolated atoms may occupy only discrete energy levels. When two atoms are placed in a molecular structure, the atomic wavefunctions ‘overlap’, splitting the atomic orbitals into separate molecular orbitals, each of a new energy. This is because, as fermions, electrons obey the Pauli exclusion principle: no two identical fermions may simultaneously occupy the same quantum state.

As additional atoms are added adjacently, available energy levels become increasingly stratified. Consequently, as the number of overlapping atomic orbitals increases, the energy difference between adjacent states decreases. This leads to *bands* of available energy levels, as well as forbidden ranges of energy: *band gaps*. Ultimately, when many atoms are bound together to form a solid lattice, the infinitesimal separation within bands is comparable with the uncertainty in energy due to the Heisenberg uncertainty principle. We may then, effectively, assume the bands to have a continuous energy spectrum[1].

4.2 Semiconductors

The conductive properties of a solid are determined by its band structure and another important parameter: the Fermi level. The Fermi level is the highest occupied hypothetical electron energy level at absolute zero temperature. Conductors, such as metals, contain a band which is partially filled and partially empty, as the Fermi level is below the top of the band. This means that there is no barrier to excitation and electrons may flow freely through the crystal.

Insulators and semiconductors have a lower energy band, which is entirely occupied, called the valence band. The Fermi level lies above this, in the band gap, which itself lies below a higher

[1] A more thorough treatment of overlapping atomic wavefunctions is approached using the linear combination of atomic orbitals LCAO. When coupled with the periodicity of crystal structures, this leads to the Bloch theorem, which explains the energy band structure of solid state materials [16, 17].

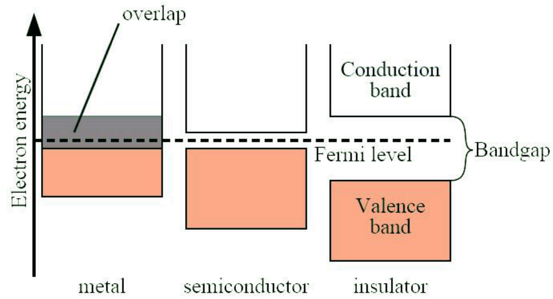

Figure 4.1: Schematic representation of the band gap difference in a metal, a semiconductor and an insulator. [18]

range of unoccupied available states known as the conduction band. The difference in energy between the top of the valence band and the bottom of the conduction band E_g corresponds to the minimum energy with which an electron must be provided in order to reach the conduction band, allowing motion across the lattice.

We can view metals too as possessing these separate bands, yet overlapping, such that this band gap energy E_g is effectively zero. For insulators this difference is significant enough that the material can be considered non-conductive. An intrinsic semiconductor has an E_g small enough such that an electron may be thermally excited in to the conduction band.

The thermal excitement of an electron from the valence band leaves behind an unoccupied state, a quasi-particle known as a 'hole'. This has a positive charge and acts, essentially, as a mobile charge carrier, with many similar properties to an electron, further contributing to a material's conductivity[2]. In thermal equilibrium there is an equal concentration of electrons n and holes p, which is in turn equivalent to the intrinsic carrier concentration n_i.

$$n = p = n_i \tag{4.1}$$

4.3 Doping

It is possible to increase the number effective mobile charge carriers by introducing impurities, or dopants, in to the crystal lattice. Such a material is an extrinsic semiconductor. The extrinsic concentration relation is then[3]:

$$n \cdot p = n_i^2 \tag{4.2}$$

An atom of Silicon provides four valence electrons that form covalent bonds with neighbouring silicon atoms. If, for example, we were to introduce a foreign Group V atom in to the lattice, the atom may donate its excess weakly bonded electron, which may easily be excited to the conduction band and cause a current. Alternatively, we could add an atom of a Group III element, accepting an electron from the lattice and thus increasing the number of holes in the valence band.

[2] Analogous to a bubble in a tube of liquid. As the liquid flows, the bubble appears to move individually, while the surrounding liquid appears stationary. Its motion may be tracked to determine the liquid's true velocity.

[3] Note that solutions to eq 4.1 satisfy eq 4.2 but not visa versa. An intrinsic semiconductor is a special case of the general formula.

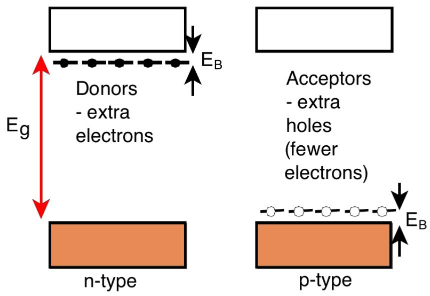

Figure 4.2: Extrinsic semiconductors: donors (acceptors) introduce energy levels just below (above) the conduction (valence) band. E_B is the energy between the nearest energy band and the additional energy states $E_B << E_g$.

In a semiconductor with an excess of donor atoms the primary mobile charge carrier is the negative electron, thus this is know as n-type. Conversely p-type semiconductors have an excess of acceptors and positive holes dominant electrical conductivity.

4.4 p-n Junctions

A p-n junction (Fig. 4.3) is merely the boundary created by a connection of p-type and n-type semiconductor material, yet forms a powerful electronic device. As the n-type has a high electron concentration and the p-type a high hole concentration, this coupling creates a diffusion gradient. Charge carriers migrate and re-combine at the junction. The n-type side now has a net positive charge (donors lose electrons) and the p-type side now has a net negative charge (acceptors gain electrons). This generates an electric field that opposes the diffusion gradient. Ultimately, when the potential across the depletion zone reaches the 'built in potential' V_{bi}, an equilibrium is formed leaving a region of low mobile charge carrier concentration, the *depletion zone* [19].

4.5 Semiconductors as Particle Detectors

Ionising particles of sufficient energy, incident on silicon crystal, will liberate electrons, resulting in the formation of electron-hole pairs. These then drift towards the anode and cathode, respectively, and the collection of the carriers allows the detection of these traversing particles. However, the probability of particle detection is reduced due to background currents: moving carriers that are not caused by high energy particles. This is predominantly caused by thermal excitation of electrons. This 'noise' masks the signal of a particles path.

In solution to this, semiconductor detectors consist principally of p-n junctions. The depletion zone acts, essentially, as a solid state ionisation chamber [21]. Due to the low background current across the depleted region, it is possible to distinguish the increase in current caused by high energy charged particles. The sensor, therefore, converts the energy deposited by a particle to an electrical signal. In the SCT, the collection of holes in the cathode, attached to the p-type silicon strips, signals a traversing charged particle (fig. 4.4).

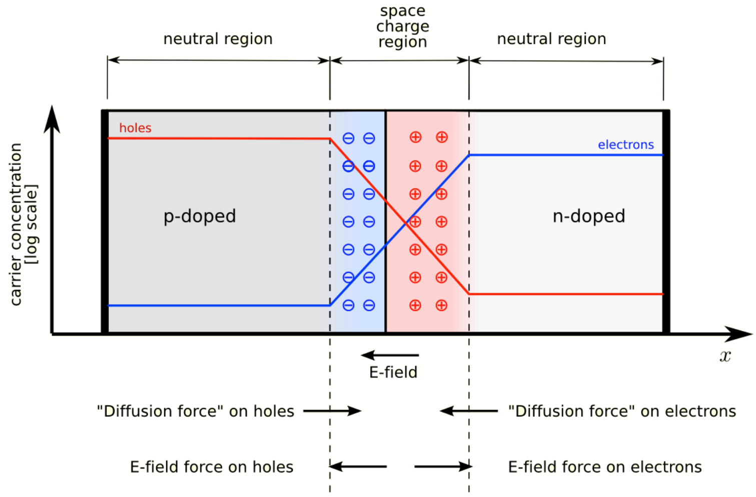

Figure 4.3: A p-n junction in equilibrium. Electron and hole concentration is indicated with blue and red lines, respectively. Grey, red, and blue regions are respectively neutrally, positively and negatively charged. [20]

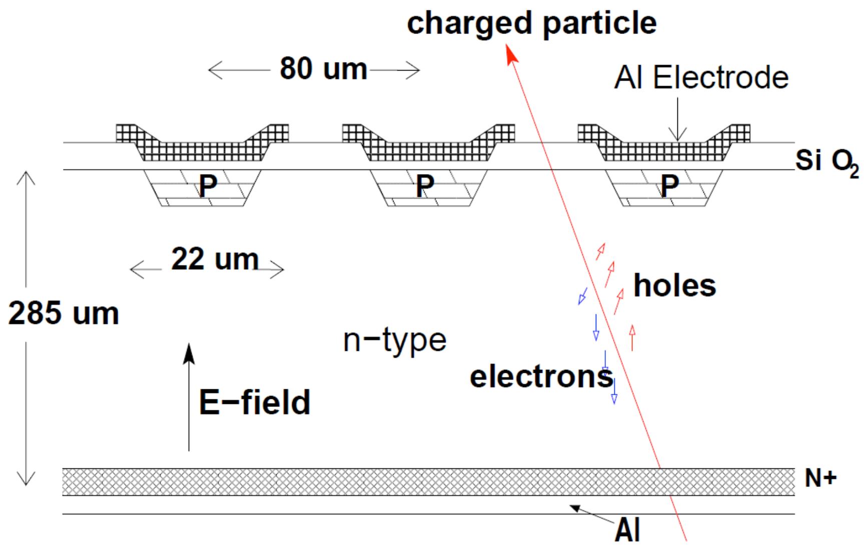

Figure 4.4: The SCT is a bulk n-type sensor, consisting of p-type silicon strips embedded in n-type silicon. A traversing charged particle creates electron-hole pairs which drift, under the electric field, towards the electrodes. The collection of holes in the aluminium electrode (cathode) connected to the p-type strips allow the detection of this particle. The reverse bias can be observed in the direction of the electric field. [6]

4.6 Depletion Voltage

Maximising the depletion width of a silicon sensor increases the probability of particle detection. To achieve this, a positive voltage is applied to the n-type side, drawing more charge carriers away from the junction. This is known as a reverse bias. The depletion voltage is the minimum potential difference required to give a depletion width across the entire sensor [21].

$$V_D = \frac{e}{2\epsilon\epsilon_0}|N_{eff}|W^2 \tag{4.3}$$

Where e is the charge of the electron, ϵ and ϵ_0 the relative permittivity and permittivity of free space, respectively. The width of the device is W. N_{eff} is the effective doping concentration, given by the difference between donor and acceptor concentrations $N_{eff} = N_{donor} - N_{acceptor}$.

4.7 Leakage Current

Ideally, in equilibrium, there would be no current across the junction. A high reverse bias, however, allows the quantum tunnelling of electrons from the valence band of the p region to the conduction band of the n region [22]. This produces a notable reverse current flow (fig 4.5).

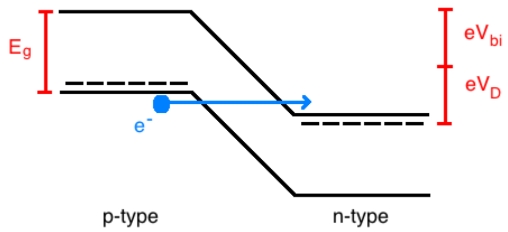

Figure 4.5: Band to band quantum tunneling for an electron in a reverse biased p-n junction. Note that an electron tunnelling from p-side to n-side is equivalent to a hole travelling in the opposite direction. In the SCT this may then be collected by the cathode. Based on [22].

Significantly, defects in the silicon crystal structure introduce additional energy levels in the band-gap, allowing the generation and recombination of electron-hole pairs across the silicon. The increased probability of thermal excitation of electrons from the valence band in to new, higher energy states increases the number of electrons which may tunnel across the junction. These factors result in a measurable current across the sensor, known as the leakage current.

This may be separated in to two categories, bulk current and surface current. Surface current is difficult to model as it is dependent on complex boundary effects in the electric field, coupled with irregularities in the silicon surface. Fortunately, bulk current is easier to theorise and most often the dominant process. Commonly, throughout this investigation, when referring to leakage current I_{leak}, it is this bulk category that is being considered. However, surface current becomes significant later in this analysis for a subset of SCT end-cap modules (Section 8.4.1).

As only defects in the depleted region affect I_{leak}, the bulk charge flow is proportional to the depletion width [21]. Therefore, for a fully depleted sensor, it is proportional to the square root of the depletion voltage itself (from eq. 4.3):

$$I_{leak} \propto W_D \propto \sqrt{V_D} \tag{4.4}$$

Predominantly, bulk current is influenced by the thermal excitation of electrons in the depleted region, it therefore has a significant temperature dependence. The ratio of the leakage current at two different silicon temperatures T_A and T_B is given by: [17]

$$\frac{I_{leak}(T_A)}{I_{leak}(T_B)} = \left(\frac{T_A}{T_B}\right)^2 exp\left[-\frac{E_g}{2k_B}\left(\frac{1}{T_A} - \frac{1}{T_B}\right)\right] \tag{4.5}$$

Where E_g is the generation energy of the silicon and k_B the Boltzmann constant. Thus, we see that leakage current decreases exponentially with decreases in temperature. In order to limit background current it is important to operate silicon detectors at low temperatures.

Chapter 5

The SCT: Semiconductor Tracker

5.1 Layout

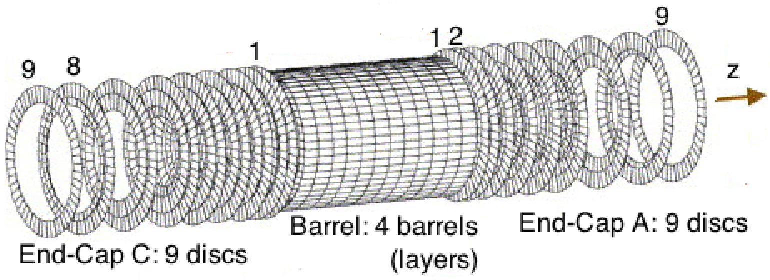

Figure 5.1: Layout of the SCT. Note the differing number of rings in each disc, as well as the orientation of modules. Edited from [23].

The Semiconductor Tracker (SCT) is the intermediate radial component of the ATLAS Inner Detector. It composes a central barrel, flanked on each side by an end-cap. Therefore, the SCT has three sections. From negative to positive z these are: End-Cap C, the Barrel (B) and End-cap A (Fig. 5.1).

The barrel composes four concentric, carbon fibre cylinders, coaxial to the beam-line. With increasing radial distance r, these are labelled barrel 3 to barrel 6[1]. Each end-cap consists of nine discs in the x-y plane, labelled disc 1 to disc 9. Disc number increases from the origin outwards along the z-axis. Encircling each disc are a maximum of three concentric rings of detector modules. These are designated, with increasing *r* the: inner, middle and outer ring (Fig. 5.2). Each end-cap has 22 individual rings of modules, the allocation of which, for each disc, can be inferred from table 5.1.

[1]Barrels 0 to 2 refer to those of the Pixel detector (Section 3.3.2).

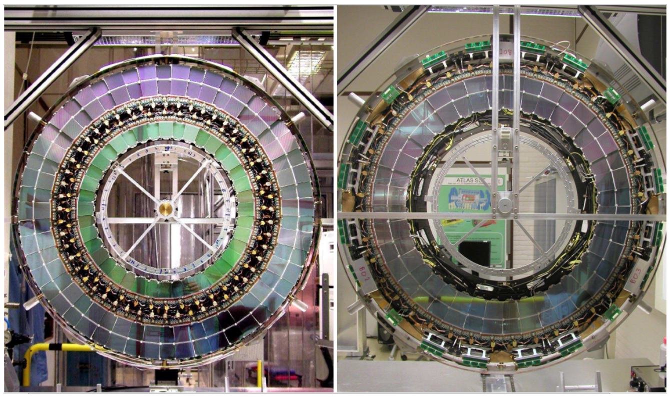

Figure 5.2: Disk 6 of End-Cap A, from both sides. Note that the inner and outer rings of modules are on one side, with the middle modules on the reverse. This imbrication provides overlap in the $r\phi$ measurements.

5.2 Modules

All end-cap detector modules comprise 'p-in-n' silicon sensors. These consist of p-type silicon strips embedded in 285 µm thick bulk n-type silicon. A number of different module designs are used throughout the SCT. All barrel modules have an identical rectangular design, while the circular shape of the end-cap discs dictate that these come in four trapezoidal species. A different species is secured around each ring and, therefore, has a corresponding name: inner, middle or outer (Fig. 5.3). Short-middle modules, the fourth species, are located only in the middle ring of disc 8. They differ solely in size and silicon area. The exact module number allocated to each ring is shown in Table 5.1. This distribution is identical for both end-caps, with 1976 modules in total.

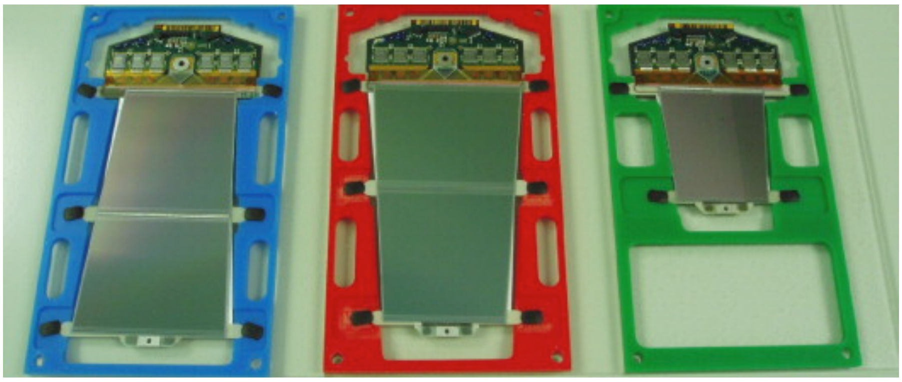

Figure 5.3: SCT End-Cap Modules. From left: Outer, Middle and Inner.

	Number of modules per ring								
Disc	**1**	**2**	**3**	**4**	**5**	**6**	**7**	**8**	**9**
Outer	52	52	52	52	52	52	52	52	52
Middle	40	40	40	40	40	40	40	40	-
Inner	-	40	40	40	40	40	-	-	-

Table 5.1: SCT module distribution across each end-cap. The red cell reports the location of the short-middle species[2] [24].

Each SCT module consists of up to four silicon sensors. These are located on both sides of the device, such that they overlap, forming a double layer of sensor material (Fig. 5.4). These sensors are manufactured to several geometries to fit each of the species and the dimensions of all are detailed in table 5.2. The sensor composition of each species, along the cumulative silicon area, is then given in table 5.3. The bulk silicon area of each module is important to consider when predicting the evolution of leakage current. The barrel sensors each have 770 silicon strips.

Additionally, when functional, modules are cooled to below 0 °C. Keeping the silicon at low temperatures is essential to minimise the detrimental effects of irradiation. Leakage current is also highly dependant on temperature, with I_{leak} decreasing exponentially for linear decreases in T_{Si} (Section 4.7). Thus, even a small reduction in temperature causes a significant improvement in minimising noise.

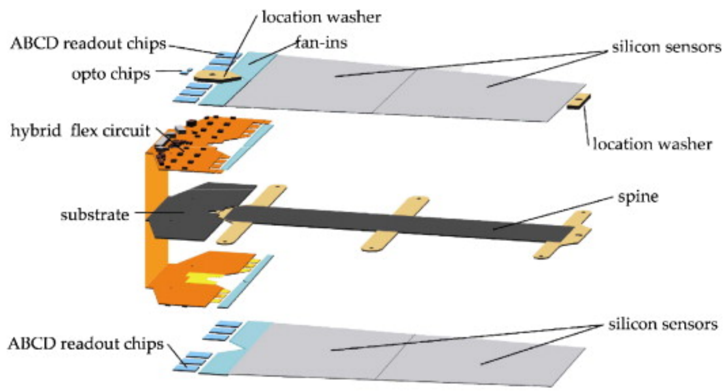

Figure 5.4: Exploded view of a SCT End-Cap middle module.

[2] Two dimensional grids, such as this, are used throughout this thesis to present information on the end-caps. Columns report discs, while rows report radial ring position. Disc number increases horizontally across columns, while radial distance from the disc centre decreases down rows. This mirrors detector geometry. The short-middle module species are added to the middle row of the grid as their radial position is the same.

Sensor Type	Outer width [mm]	Inner Width [mm]	Length [mm]	Area [cm^2]
Forward W12	55.488	45.735	61.060	30.903
Forward W21	66.130	55.734	65.085	39.658
Forward W22	74.847	66.152	54.435	38.376
Forward W31	64.636	56.475	65.540	39.688
Forward W32	71.814	64.653	57.515	39.244
Barrel W00	63.560	63.560	63.960	40.653

Table 5.2: SCT sensor dimensions [24].

Module	Silicon Sensors	Silicon Area [cm^2]
Outer	$2 \times W32 + 2 \times W31$	157.865
Middle	$2 \times W22 + 2 \times W32$	156.068
Short-middle	$2 \times W22$	76.753
Inner	$2 \times W12$	61.807
Barrel	$4 \times W00$	162.612

Table 5.3: SCT module dimensions.

5.3 SCT Requirements - A Fermi Estimate

The SCT occupies a radial range between 30 and 52 cm. The barrel of the SCT has an $|\eta|$ coverage of ± 1.4, while the end-caps cover the forward region from 1.7 to 2.5. At a luminosity of $1 \times 10^{27}\,\mathrm{cm^{-2}\,s^{-1}}$ and bunch spacing of 25 ns, every bunch crossing typically results in the emergence of around 1000 particles with $|\eta| < 2.5$. Luminosity may be increased as high as $3 \times 10^{27}\,\mathrm{cm^{-2}\,s^{-1}}$, creating even higher flux densities.

In order to reconstruct the interactions that produced them, and extract the relevant signals for new physics processes, it is necessary to determine the tracks of all emerging charged particles. Its close proximity makes it particularly important in the identification of short-lived, rapidly decaying particles.

This relies on high precision measurements of position at small radius, especially for when particle flux density is high. The SCT is designed to fulfil this function. Featured below is a simple estimation of the required resolution for the SCT [6].

A singly charged classical particle bending in a magnetic field B may be described by equating the force upon it, due to B, and the centripetal force of its rotation. Cancelling like terms and rearranging for the radius of curvature gives:

$$r = \frac{p}{eB}. \tag{5.1}$$

Where p is the momentum of the particle. Assuming an ultra-relativistic particle with an energy of 1 TeV and $\eta = 0$, then (accounting for units):

$$r = \frac{p}{0.3 \times B} = \frac{10^3\,\mathrm{GeV}}{0.3 \times 2\,\mathrm{T}} = 1660\,\mathrm{m} \tag{5.2}$$

In order to determine the sign of the charge we must be able to resolve the sagitta (arc depth) of the particle's path s. This depends on the length of the base of the arc L. For the SCT, at $\eta = 0$ this is equal to the radial distance of the outer barrel at 52 cm. Thus, as $r >> s$, s is approximated by:

$$s \approx \frac{L^2}{8r} = \frac{0.52^2\,\mathrm{m}^2}{2 \times 1660\,\mathrm{m}} = 20\,\mu\mathrm{m} \tag{5.3}$$

Hence, to determine the sagitta of the particle, each SCT space-point measurement should have a resolution of less than 20 μm in the bending direction. In the electric field across the sensor, liberated charge carriers drift directly towards the strips and are then swept to the electrodes. This system has an essentially box-like response function, with a resolution equal to the distance between electrodes d [25]. However, a particle's path is randomly aligned with respect to any strip, therefore, the difference between the measured and the true position has a Gaussian distribution, with a deviance of:

$$\sigma^2 = \frac{1}{d} \int_{-d/2}^{d/2} x^2\,\mathrm{d}x = \frac{d^2}{12} \tag{5.4}$$

A factor of $\sqrt{2}$ also arises due to the two independent strip measurements. Therefore, the relation between the resolution and d is:

$$resolution = \frac{1}{\sqrt{2}} \frac{d}{\sqrt{12}} \tag{5.5}$$

Rearranging for d and substituting the resolution from eq. 5.3:

$$d = \sqrt{24} \times 20\,\mu\mathrm{m} \approx 100\,\mu\mathrm{m} \tag{5.6}$$

Hence d should be less than 100 μm to determine the sagitta of the particle. This parameter is also the inter-strip distance, known as the pitch.

5.4 Contribution to Event Reconstruction

With a pitch of approximately 80 μm (Fig. 4.4), the SCT has the high granularity necessary to resolve the tracks of high energy particles. The system provides an $r\phi$ resolution per measurement of 16 μm. The sensor on one side of a module is also rotated by a small stereo angle of 40 mrad from the sensor on the opposing side. This provides a positional resolution of 580 μm along z or r in the barrel or end-caps, respectively.

The sensor system has a binary read out, for each time slot, a strip may register only a 'miss' or a 'hit'. Aside from the lower data transmission requirements, this system requires less power than the analogue alternative, which, therefore, aids in cooling. The threshold current that a particle must deposit for a hit is 1 fC. This minimises false hits caused by background currents, granting a hit efficiency of greater than 99%.

Particles pass through multiple sensors as they emerge from the interaction point. This then provides several position measurements along the trajectory of each particle. A particle traversing the barrel of the SCT can register a potential total of eight hits: two strip hits for every module, in each of the four barrels. To determine isolated tracks for each particle, such that they can be identified from the sea of hits, a precision measurement is required in each layer of the detector.

This allows computational algorithms to process the hits and fit tracks, which, ultimately, may be used to accurately determine the vertices of the interactions [26]. The goodness-of-fit for each track determines how well the algorithm can apply the curve of a particles trajectory to a pattern of SCT hits[3]. Obviously, this has a dependency on the number of precision SCT hits and a minimum of six must be identified for a single track in order for the algorithm to be applied effectively. High granularity is especially important when the particle flux density is high.

Establishing the interaction vertex of each particle is of obvious importance in determining the processes that led to its production. As an example, many physics analyses cut particle entries with fewer than seven SCT hits and those with otherwise low goodness-of-fit. Specifically, if the hit efficiency of the end-caps were to decrease, then tracking high η particles would become less reliable and reduce the hermicity of the detector. Therefore, to ensure accurate tracking, vertex identification and overall hermeticity, the high hit efficiency must be maintained. This includes limiting the noise in the modules due to anomalous currents, and thus monitoring the effect of radiation damage on the leakage current of the sensors.

[3]Specifically the method used to determine the goodness-of-fit of a track to a sequence of hits in the inner detector is the χ^2 test.

Chapter 6

Radiation Damage of Semiconductor Detectors

An incident high energy particle may cause radiation damage via two principle mechanisms: surface and bulk. Surface damage corresponds to ionisation caused by charged particles inelastically scattering with lattice electrons. Bulk damage can arise due to both neutral and charged particles. It is caused by elastic scattering and results in the removal of atoms from lattice sites. This later process is dominant and the principle limiting factor for silicon detectors in a high radiation field, close to particle interaction points. Thus, it is the sole process considered henceforth [21].

6.1 Bulk Radiation Damage

The mechanism of bulk damage in silicon is initialised by the the removal of an atom due to incident radiation. The dislodged atom is a primary knock-on atom (PKA) and the resulting vacant lattice site forms an interstitial defect in the crystal. The PKA and the interstitial together form a Frenkel Pair. This may simply result in a stable defect, yet if the PKA has sufficient energy it can go on to remove additional atoms creating clusters of Frenkel pairs. PKAs and vacancies can also transverse the lattice and may recombine after their initial displacement [27].

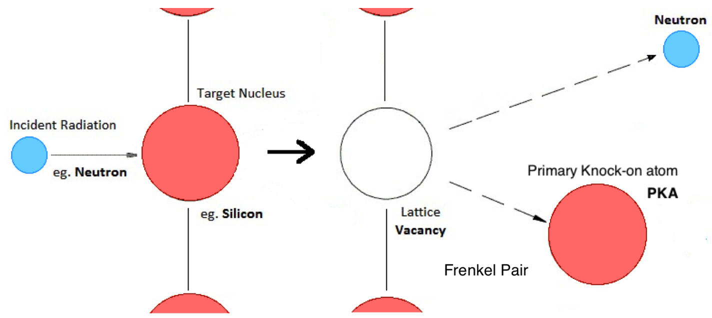

Figure 6.1: Bulk radiation damage

6.2 NIEL: The Non-Ionising Energy Loss Hypothesis

Ideally, it is desired to quantify all radiation damage to the silicon. This may appear difficult, as the incident particles have a high multiplicity. However, bulk damage is charge independent and the Non-Ionising Energy Loss hypothesis (NIEL) may be utilised.

NIEL asserts that, after the initial collision, all subsequent damage processes are caused by the PKA. Consequently, damage scales linearly with the initial energy transferred by the incident particle. This then allows the normalisation of all forms of radiation damage to a standardised dose. This is chosen to be the damage caused by a neutron with kinetic energy of 1 MeV to area of $1\,\mathrm{cm}^2$. This quantity is the time integrated neutron flux or fluence Φ, with units of $1\,\mathrm{MeVn_{eq}cm^{-2}}$.

6.3 Annealing

After a period of irradiation, the semiconductor can undergo a number of annealing processes. In the short term the material undergoes beneficial annealing. Due to thermal excitation, defects can move through the crystal and migrate back to stable configurations, restoring the original crystal lattice structure. As this process is dependant on thermal motion, a higher temperature results in more rapid beneficial annealing. On longer time scales the semiconductor will undergo reverse annealing which results from the formation of dense clusters of interstitial defects and acts, principally, to reduce the effective doping concentration, with no significant affect on leakage current [21].

6.4 Radiation and Depletion Voltage

Bulk radiation damage results in the removal of donors and generation of acceptors in the silicon lattice and, therefore, reduces the effective doping concentration N_{eff}. This then directly affects the depletion voltage V_D of the sensor (eq. 4.3). The SCT bulk silicon was originally n-type, with a high concentration of donors. The removal of these dopants results in an initial decrease in V_D, dropping until both it and N_{eff} are equal to zero. The continuing generation of acceptors now causes N_{eff} to becomes negative. This means that the n-type becomes p-type, a process known as type-conversion. The depletion voltage then increases for the remainder of the sensor's functional lifetime. Therefore, an increasingly high reverse-bias V_R is necessary to pull charge carriers from the p-n junction.

When $V_D > V_R$ the sensor is no longer fully depleted, the sensitive region of the silicon retreats and the efficiency of the SCT is reduced. Reverse annealing is a significant factor in depletion voltage evolution. In order to guarantee the full depletion of the device, it is necessary that the depletion voltage be kept below the limited reverse bias of the power supply.

Initially, the depletion voltage of the SCT modules was 65 V, with a reverse bias of 150 V. This ensures that $V_D < V_R$, yet is not so high as to cause breakdown of the sensor. The depletion voltage of the SCT sensors is not directly the subject of this study. However, leakage current evolution is an indicator of the scale of overall radiation damage, and, therefore, measurements consistent with theoretical evolution suggest that the depletion voltage is developing similarly.

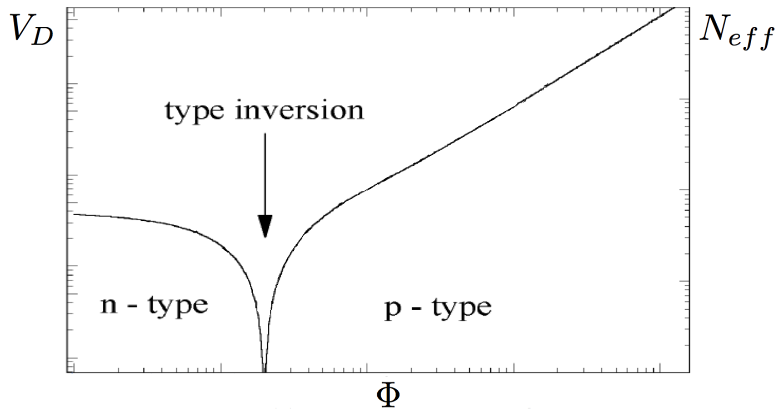

Figure 6.2: Example of type inversion in irradiated silicon. Note the logarithmic scale. Edited from [28].

6.5 Radiation and Leakage Current

As seen in section 4.1, the leakage current of a sensor is heavily dependent on lattice defects. Radiation induced interstitial defects result in additional energy states within the band gap. These allow the generation and recombination of electron-hole pairs and thus act to increase the concentration of charge carriers moving across the p-n interface. As a result, increases in leakage current per unit volume increase directly proportionally with increases in radiative fluence [21].

$$\Delta I_{leak} = \alpha V \Delta\Phi \tag{6.1}$$

V is the effective volume of the silicon. ΔI_{leak} and $\Delta\Phi$ are the change in leakage current and fluence, respectively. α is the proportionality factor, the 'current related damage rate'.

6.6 HM: The Harper Model

A model of leakage current evolution, considering annealing processes, was developed by R. Harper and featured in his 2001 Ph.D. thesis for Sheffield University [29]. The predictive model contains numerous variables that have been determined experimentally and its overall structure has been tailored around the observed evolution of numerous semiconducting materials. It specifies the current related damage rate α, taking in to consideration temperature, annealing and the history of irradiation.

$$\Delta I_{leak} = \alpha(\Theta(T_H)t_{ir}, \Theta(T_H)t')V\Delta\Phi \tag{6.2}$$

Whilst reverse annealing of the silicon factors in the evolution of depletion voltage, the HM does not have a term relating to this process, only beneficial annealing is seen to influence leakage current evolution and thus factors in α.

This evolution can be expressed as a summation of exponential terms, with the form of α given by:

$$\alpha(\Theta(T_H)t_{ir}, \Theta(T_H)t') = \alpha_{eq}(T_H)\sum_{i=1}^{n}\left\{A_i \frac{\tau_i}{\Theta(T_H)t_{ir}}\left[1 - exp\left(-\frac{\Theta(T_H)t_{ir}}{\tau_i}\right)\right] exp\left(-\frac{\theta(T_H)t'}{\tau_i}\right)\right\} \tag{6.3}$$

Here t_{ir} is the time duration of the irradiation, while t' is the time since irradiation. Also important are the amplitudes A_i and time constants τ_i. $\theta(T_H)$ is a scaling term between the reference temperature of the variables $T_R = 293.15\,\text{K}$ and the temperature at which Harper conducted his experiments $T_H = 266.15\,\text{K}$, given by:

$$\Theta(T_H) = exp\left[-\frac{E_I}{k_B}\left(\frac{1}{T_H} - \frac{1}{T_R}\right)\right] \tag{6.4}$$

Where $E_I = 1.09\,\text{eV}$ is the activation energy for the silicon in Harper's Study.

In order to use this model for successive leakage current predictions it is necessary to manipulate it in to an iterative form, such that[1]:

$$I = \sum_{j=0}^{N} \Delta I_j \tag{6.5}$$

With $\Delta I_0 = I(t = 0)$ being the original leakage current. The series index j reflects the history dependence of the system. The evolution can be expressed as a potentially infinite summation of exponential terms. The HM includes the first five terms of the series:

$$\Delta I_j(T_{Si}) = \Gamma(T_{Si})\sum_{i=1}^{5} \Delta I_j^i \tag{6.6}$$

Manipulating equation 6.3, these then have the following iterative form:

$$\Delta I_j^i(\Delta\Phi, \Theta(T_H), t) = exp\left[-\frac{\Theta(T_H)t}{\tau_i}\right]\Delta I_{j-1}^i + \alpha_{eq}(T_H)A_i\frac{\tau_i}{\Theta(T_H)t}\left(1 - exp\left[-\frac{\Theta(T_H)t}{\tau_i}\right]\right)V\Delta\Phi_j \tag{6.7}$$

Where t is the time since the previous iteration[2]. Each one, indexed in i, has an associated amplitude A_i and time constant τ_i, the values of these are listed in table 6.1. V is the volume of the sensor and $\alpha_{eq}(T_A) = 7 \times 10^{-18}\,\text{A cm}^{-1}$ is the current related damage rate. $\Delta\Phi_j$ is simply defined as:

$$\Delta\Phi_j = \Phi_j - \Phi_{j-1} \tag{6.8}$$

[1]Presently dropping the leak subscript $I = I_{leak}$

[2]Later, when making predictions, a consistent granularity of one day is used.

The purpose of the factor Γ (Eq. 6.6) is to correct the leakage current from Harper's experimental temperature to the temperature (T_{Si}) of the SCT silicon[3]. It takes its form from equation 4.5:

$$\Gamma(T_{Si}) = \left(\frac{T_{Si}}{T_H}\right)^2 exp\left[-\frac{E_g}{2k_B}\left(\frac{1}{T_{Si}} - \frac{1}{T_H}\right)\right] \tag{6.9}$$

Where $E_g = 1.21\,\text{eV}$ is the effective band gap, or the generation energy of electron-hole pairs in the silicon of the SCT modules [30].

i	A_i	τ_i (days)
1	0.42	833.33
2	0.10	28.47
3	0.23	2.57
4	0.21	0.09
5	0.04	0.01

Table 6.1: Harper model amplitudes and time constants [31].

Any unspecified units used above were: degrees Kelvin (K) for temperature, days for time, centimetres (cm) for distance and electron volts (eV) for energies.

6.7 Importance of Understanding Leakage Current Evolution

In section 5.4 the contribution of the SCT to the reconstruction of high energy events is detailed. The emphasis being on high single point precision measurements in order to accurately fit tracks to the paths of traversing particles. This high precision relies upon an excellent individual hit efficiency of greater than 99%.

Leakage current I_{leak} is, effectively, noise that masks the signal attributable to these particles. Therefore, an increase in leakage current effectively acts to reduce the goodness-of-fit of the resulting tracks. For small increases, this effect is limited due to the binary readout of the SCT. However, critical increases in the leakage current of the sensors can be catastrophic by triggering thermal runaway.

This arises because increases in leakage current act to increase device temperature T_{Si}, due to the electrical resistance of the silicon. At a critical point, this prompts spontaneous thermal excitation of electrons from the valence band to the conduction band. In the depletion zone this results in a larger I_{leak} [21], which feeds back to increase T_{Si}. Ultimately, the runaway current makes a signal impossible to resolve. It is, therefore, important to keep module T_{Si}, and I_{leak} below this critical point. The maximum permissible leakage current is 5 mA [1].

In addition to this, I_{leak} is a good indicator of the absolute bulk radiation damage, which influences other detector properties, such as the depletion voltage (Section 6.4). It is also considerably easier to observe directly than the alternative parameters.

[3] Or, as used later, a normalisation temperature, taken as 0 °C.

The SCT has been developed to account for the effects of silicon irradiation. This includes long term predictions of leakage current evolution, from installation, until the proposed end-of-life of the ATLAS detector. The expected end-of-life leakage current was estimated at around $2-3$mA [2]. Therefore, a safety factor of approximately 2 was established. This should ensure that the SCT functions successfully for the duration of data collection.

However, therefore, the findings of the 2010 study, with regional discrepancies in $R_{leak} = I_{data}/I_{HM}$ of approximately 2, pose a significant problem (Section 1.2). The subject of this analysis is the subsequent evolution in leakage current in order to investigate this phenomenon.

Chapter 7

Predicting the Evolution of Leakage Current

7.1 Aims of predictions

The aim of these predictions is to model the evolution of leakage current for each module of the SCT end-caps, using the Harper Model (section 6.6). The evolution for the barrel modules is also calculated. This is so that the comparisons with data may be compared to a parallel study performed by T. Kondo on this central SCT section [32]. The aim of this is to test the validity of the procedure used to evaluate the end-caps.

The primary variables of the HM are the radiative fluence and the semiconductor temperature. The dimensions of the modules are also important, these are detailed in section 5.2. Following are details of all the input parameters used with the Harper model in this analysis. The software used to generate predictions from these inputs was developed by J. Roberts, of the University of Southampton, as part of his Master of Physics thesis [31].

7.2 Fluence Per Unit Integrated Luminosity

The fluence incident on each SCT module can be divided in to two independent inputs using the following relationship:

$$\Delta\Phi = \phi\Delta L \tag{7.1}$$

Where L is the integrated luminosity and ϕ is the fluence per unit integrated luminosity[1]. This independence is useful, as integrated luminosity is a common property for the entire LHC and ϕ is a constant for a given detector region[2]and collision energy.

The fluence per unit integrated luminosity effectively quantises the 'amount' of radiation that has been incident on the device (Section 6.2) for a given integrated luminosity. Calculating the

[1]Henceforth, for convenience, 'fluence' commonly refers to the 'fluence per unit integrated luminosity'.

[2]Commonly during this analysis, the term 'region' of the SCT refers, specifically, to areas that receive a uniform fluence according to FLUKA. i.e. all modules in an SCT region are subject to equal irradiation per unit area.

fluence received across each region of the detector is highly complex, affected by the geometry of the detector and the interactions between the produced particles, as well as with the detector subsystems. It is, therefore, necessary to model the fluence using intricate Monte Carlo simulations.

Due to the cylindrical symmetry of ATLAS in general, and the SCT subsystem in particular, the magnitude of fluence for given regions is, effectively, theoretically identical. For the Barrel, this means that all the modules for a given layer receive the same fluence, while, in the end-cap, this symmetry means that the same can said of all the modules around a given ring of a given disc. The fluence per unit integrated luminosity for each of these regions was generated using a combination of Pythia 8 and FLUKA[3]Monte Carlo event simulations, with both 7 TeV and 8 TeV collisions [33]. The 7 TeV fluences account for 2010 and 2011 LHC running. In 2012 the collision energy of the LHC was increased to 8 TeV, universally increasing the irradiation of all regions. This information can be found in tables 7.1 and 7.2 for the barrel and end-caps, respectively.

The simulations take in to account all detector elements, their masses and radiation lengths, as well as the particle behaviour and interactions. The influence of the processes that, as considered by these algorithms, particularly affect the fluence may be observed in the results. Most apparently, fluence is influenced by proximity to the beam-line [36], with the closest regions receiving the highest dose. Naively, it might be expected that the modules on discs at the greatest radius spherically from the collision point, and cylindrically from the beam-line, would receive the highest irradiation. However, this is clearly not observed, with a general trend of increasing fluence with increasing $|z|$.

	ϕ [10^{11} MeVn_{eq}cm^{-2}fb^{-1}]	
Layer	**7TeV**	**8TeV**
B6	0.92	0.97
B5	1.07	1.13
B4	1.30	1.37
B3	1.65	1.74

Table 7.1: Fluence per unit integrated luminosity ϕ averaged over each barrel layer.[33]

[3]Pythia is a Monte Carlo for the generation of high-energy collisions, which physically models (in vacuo) scattering processes and the evolution to complex high multiplicity final states. FLUKA Monte Carlo then simulates the interaction of the produced particles with detector material [34, 35].

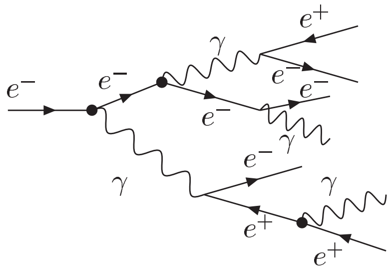

Figure 7.1: A Feynman diagram of an electromagnetic particle shower.

	ϕ [10^{11} MeVn_{eq}cm^{-2}fb^{-1}]								
Disc	**1**	**2**	**3**	**4**	**5**	**6**	**7**	**8**	**9**
Outer	1.04	1.02	1.03	1.06	1.08	1.15	1.26	1.47	1.68
Middle	1.28	1.27	1.29	1.30	1.35	1.41	1.54	1.79	-
Inner	-	1.66	1.67	1.69	1.70	1.79	-	-	-

(a) **7TeV**

	ϕ [10^{11} MeVn_{eq}cm^{-2}fb^{-1}]								
Disc	**1**	**2**	**3**	**4**	**5**	**6**	**7**	**8**	**9**
Outer	1.09	1.09	1.08	1.11	1.13	1.21	1.34	1.56	1.78
Middle	1.36	1.35	1.35	1.40	1.41	1.49	1.64	1.91	-
Inner	-	1.76	1.74	1.79	1.83	1.90	-	-	-

(b) **8TeV**

Table 7.2: Fluence per unit integrated luminosity ϕ averaged over each end-cap ring.[33]

7.2.1 Particle Showering

Particle showering effects are due to high energy particles interacting with the dense material of the detector systems and producing cascades of secondary particles. Particle showers can be split in to two categories: Electromagnetic and Hadronic. The second category of showers are dominated by successive inelastic hadronic interactions. At high energy, these are characterized by excited nuclei undergoing nuclear decay, resulting in multi-particle production. Products are made up predominantly of nucleons and pions.

Electromagnetic showers are caused by particles that interact primarily via electromagnetism EM. Charged particles undergo deceleration when deflected by the electric field of an another charged particle. bremsstrahlung refers to the photon that is emitted by the decelerating particle, in order to conserve energy, as well as to the process itself. In the case where acceleration is perpendicular to the velocity of the particle, such as in a synchrotron, the radiated power P is given by [37]:

$$P = \frac{\mu_0 q^2 a^2 \gamma^4}{6\pi c} \tag{7.2}$$

Where q is the charge of the particle, a the acceleration and γ is given in equation 3.3. It follows that the energy lost in bremsstrahlung is proportional to the inverse-fourth-power of the mass. For high-energy electrons travelling through a dense medium and interacting with atomic nuclei, this is the dominant form of energy loss[4].

The emitted photons, of sufficient energy, may then undergo electron-positron pair production, through interaction with a nucleus. Participation of the nucleus is required in order to satisfy the energy and momentum conservation laws [38]. The electron and positron products can then, themselves, undergo bremsstrahlung. The interplay of these two processes forms the primary source of EM showers (fig. 7.1). This continues until the photon energy falls below the threshold for pair production, at which point, lower energy electromagnetic interactions remain, such as Compton scattering and the photoelectric effect [39].

Scattering processes occur dominantly in the calorimeter system (Section 3.3.3), where they are utilised in the absorption and resulting measurement of the energy of traversing particles. The products of these showers are emitted in many directions and, therefore, particulary at large $|z|$ and r, can propagate back in to the inner detector. It is largely the influence of these processes that determines the fluence distribution of the SCT, as reflected in the FLUKA Monte Carlo results.

7.3 Integrated Luminosity

Luminosity $\mathcal{L}$ is the proportionality factor between the rate of scattering events $\dot{N} = dN/dt$ and the production cross section for this event σ:

$$\dot{N} = \mathcal{L} \cdot \sigma \tag{7.3}$$

In the LHC, each beam acts, simultaneously, as both target and incident beam. Assuming a head on collision of identical, ultra-relativistic proton beams, with number of protons per bunch N_x, bunches per beam n, revolution frequency f and beam cross section A, the luminosity is given by[5] [5, 40, 41]:

$$\mathcal{L} = f \frac{n N_x^2}{A} \tag{7.4}$$

The integrated luminosity[6] is merely the luminosity integrated over time:

$$L = \int \mathcal{L} \, dt \tag{7.5}$$

[4]This is also the reason that muons may traverse the dense material of the calorimeter system without absorption: $\frac{P_e}{P_\mu} = \left(\frac{m_\mu}{m_e}\right)^4 \approx 10^9$.

[5]Substituting very approximate numbers from chapter 2: $L \approx \frac{(10^{11})^2 \times 2{,}800 \times 11{,}000\,\mathrm{Hz}}{5 \times 10^{-6}\,\mathrm{cm}^2} \approx 10^{34}\mathrm{cm}^{-2}\mathrm{s}^{-1}$

[6]Henceforth, 'luminosity' commonly refers to the 'integrated luminosity' L.

As shown in equation 7.1, the absolute fluence incident on each part of the detector is directly proportional to the luminosity. It has been also been demonstrated that the proton-proton collision luminosity is the dominant contribution to the irradiation of the SCT [2]. Due to the history dependence of leakage current evolution, it is important to know the luminosity for each increment of the predictions.

Therefore, the integrated luminosity profiles used in calculating leakage current are constructed from the daily stable proton-proton collision luminosity recorded in 2010, 2011 and 2012 [42]. The total integrated pp luminosity delivered to ATLAS over these three years reached almost $29\,\mathrm{fb}^{-1}$. Plots of total integrated luminosity per day, cumulatively summed, are displayed in figure 7.2 with both linear and logarithmic scales. There is also a relative error in the luminosity of ± 0.02, which is accounted for in the final uncertainty of the predictions.

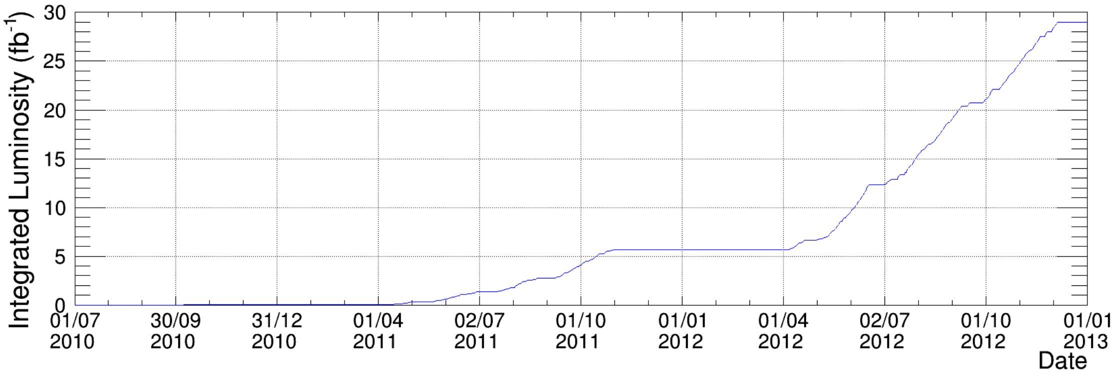

(a) Linear scale

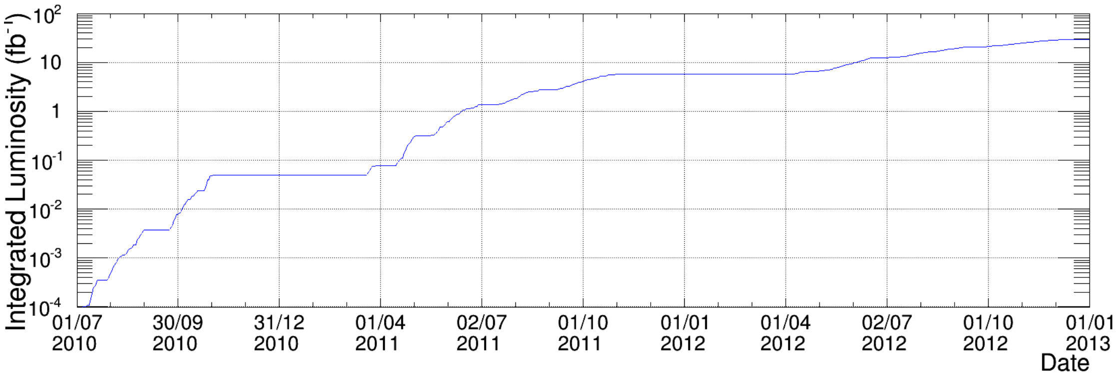

(b) Logarithmic scale

Figure 7.2: Profile of total Integrated luminosity per day, cumulatively summed. This was constructed from daily results for stable pp collision luminosity delivered to point 1 in 2010, 2011 and 2012 [42].

7.4 Temperature

As can be seen in figure 5.4, each module possesses a processing chip called the 'hybrid flex circuit'. This chip performs multiple functions in data handling for the device, as well as monitoring the device temperature. However, it has been shown that there is a disparity between the chip temperature and the silicon temperature. This is particularly true for the end-caps, due to a loose thermal coupling between chip and bulk silicon, resulting in systematic differences in some rings of greater than 15 °C [43].

The result of this is that precise temperature profiles for each module are presently impossible to determine. For the purpose of this investigation, regional assumptions of temperature have been made with the information available.

As discussed, respectively, in sections 4.7 and 6.5, temperature has an effect on both immediate leakage current and its evolution under irradiation. In order to limit both these factors and minimise noise, the temperature of the SCT modules should be kept as low possible. Balancing the limits in cooling systems with gains in radiation hardening and noise reduction, the intended temperature of the modules is -7 °C or below [44]. -7 °C is, therefore, the nominal functional temperature for the modules of the SCT.

Maintaining this consistent temperature, however, is challenging. Cooling is accomplished using an evaporative system and there are unavoidable differences in pressure between each SCT section. There are also differences in the cooling liquid itself. This means that the average silicon temperatures across all SCT regions are not uniform. There are also temperature variations module-by-module.

Due to pressure differences between forward and central regions, the module temperatures of the inner three barrel layers are higher than optimal, at approximately -2 °C. Barrel 6 is at an even high temperature of 5 °C[7]. There is an uncertainty due to module-by-module fluctuations of ± 0.5 °C.

For the end-caps, a consistent functional silicon temperature at the nominal -7 °C is assumed, though the complications in data acquisition for these modules make this conjectural. The uncertainty due to the ring-by-ring differences, and the module by module fluctuations, is ±1 °C. When the SCT is undergoing maintenance, modules are warmed to 17 °C. This information is summarised in table 7.3. Combined with the known periods of time during which modules are undergoing maintenance and during which they are functional [32], temperature profiles for the sensors of each region are assembled. These are displayed in figure 7.3.

	T_{Si} [°C]	
Module Location	Functional	Maintenance
End-Cap	-7.0 ± 1.0	$+17.0$
B3, B4, B5	-2.0 ± 0.5	$+17.0$
B6	$+5.0 \pm 0.5$	$+17.0$

Table 7.3: Summary of SCT module Silicon Temperature assumptions.

[7] The surrounding TRT requires a higher functional temperature than the SCT. The outer layer (Barrel 6) deliberately compensates for a partial failure of the heat shield between it and the TRT, preventing the TRT freezing due to heat exchange.

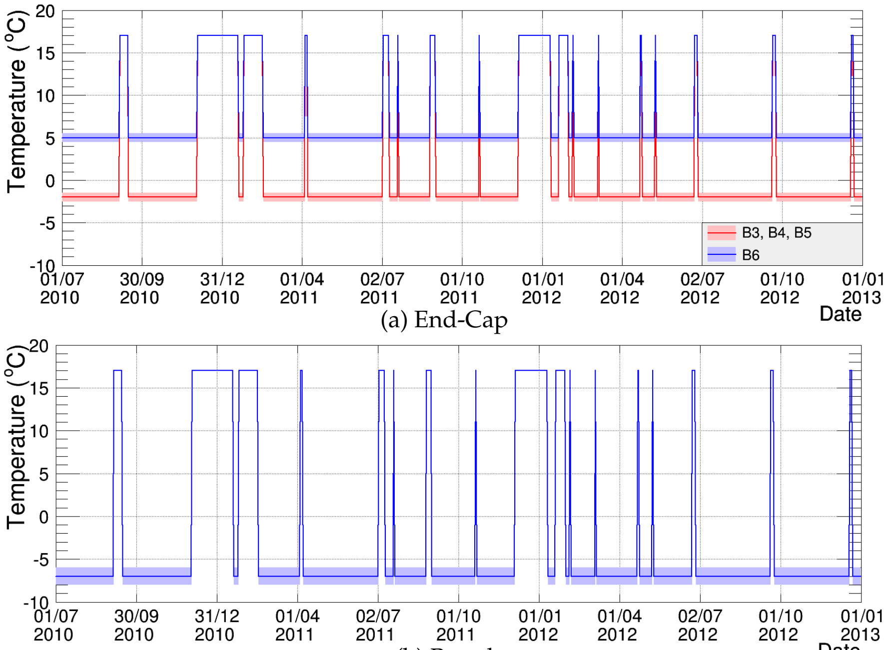

(a) End-Cap

(b) Barrel

Figure 7.3: Temperature profile for the barrel and end-cap, showing fluctuation between operation and maintenance temperatures.

7.5 Output

Due to the common module properties and detector symmetry, the predictions for modules from certain regions of the detector share the same theoretical evolution. This is predominantly due to the shared fluence per unit integrated luminosity for each barrel layer and end-cap ring. Thus, separate predictions must be made for all 22 end-cap rings: each ring of each disc, as well as for each of the 4 barrels.

Plots of the resulting theoretical evolution for the barrel and end-cap are shown in figures 7.4 and 7.5. As explained above, these are made with a granularity of one day. Note that these are the 'normalised' predictions. This means that as part of the Harper model calculation (Section 6.6), rather than being scaled to the absolute silicon temperature of the SCT, they have been scaled to 0 °C, with the volume set to 1 cm^3. Therefore, instead of the leakage current per module, the equivalent leakage current at 0 °C per unit volume (I_{leak} @ 0 °C [μA/cm^3]) is used. This was the standard agreed upon by four LHC experiments in order to compare the radiation damage of multiple subsystems, operating at varying temperatures, such that the effect of fluence is highlighted.

The plots feature the uncertainty in the predictions as lighter bands of colour surrounding the line of evolution. This uncertainty is due to the uncertainty in temperature and luminosity, added in quadrature. The later is by far the lesser factor. Due to the highly non-linear relationship between leakage current and temperature, this final uncertainty is asymmetric. Uncertainty in the Harper model amplitudes and time constants, as well as in the Monte Carlo fluences, have not been accounted for.

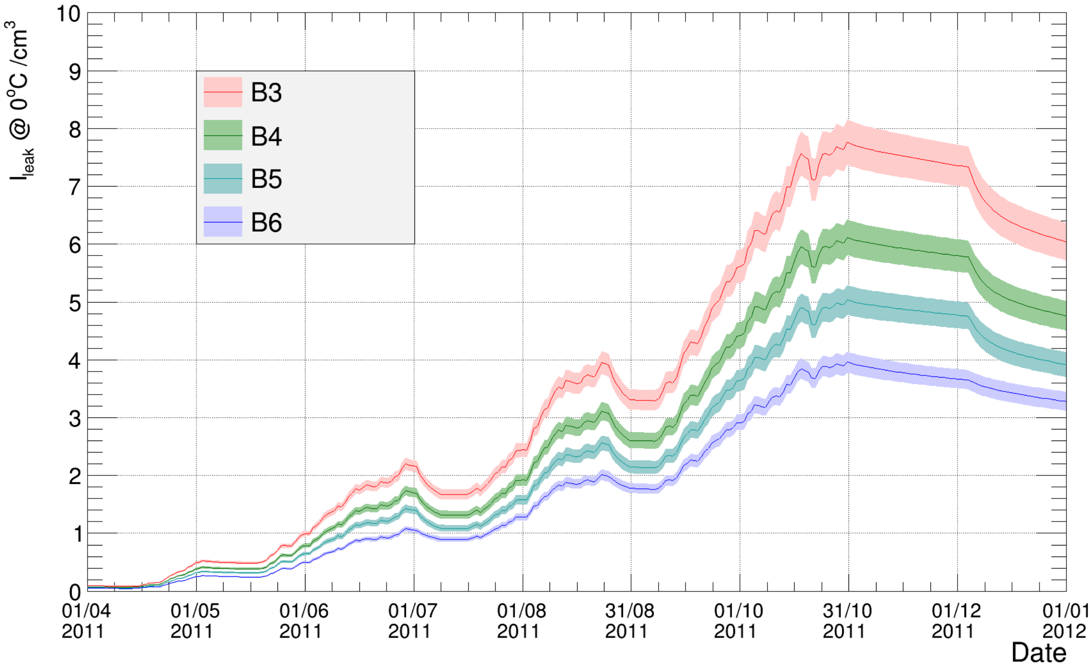

(a) Normal scale

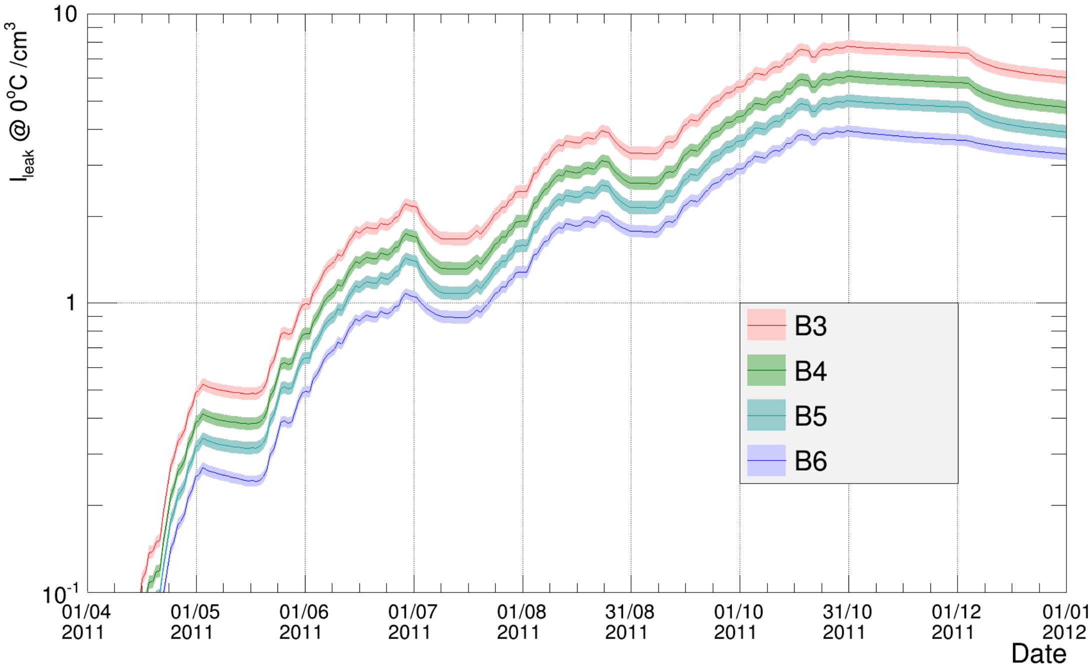

(b) Logarithmic Scale

Figure 7.4: Predicted Leakage current evolution for all layers of the Barrel.

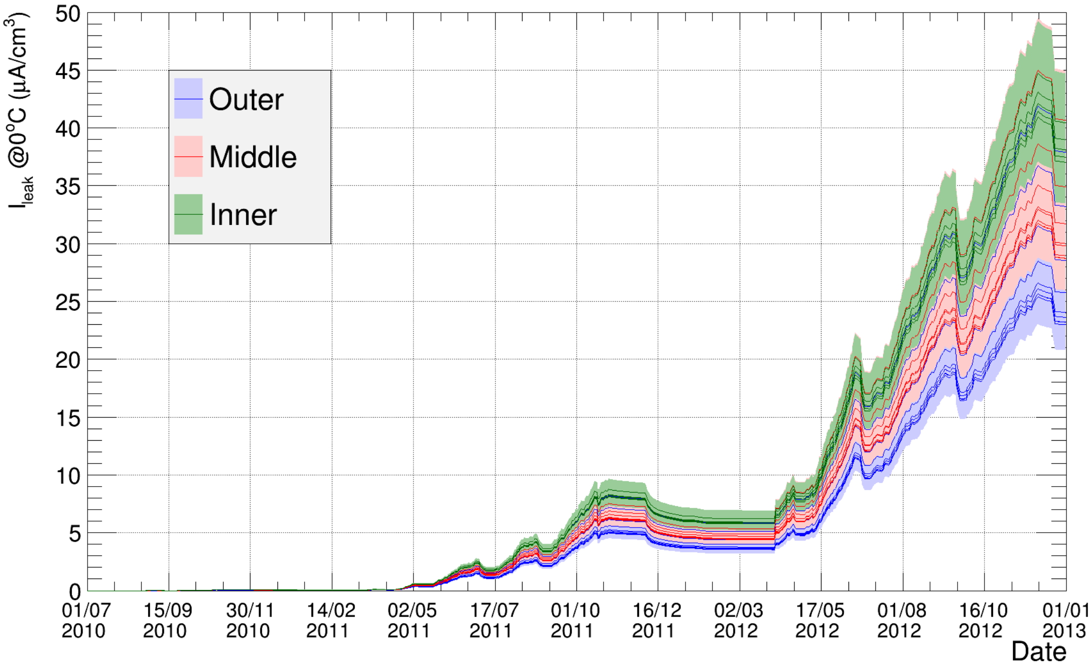

(a) Normal scale

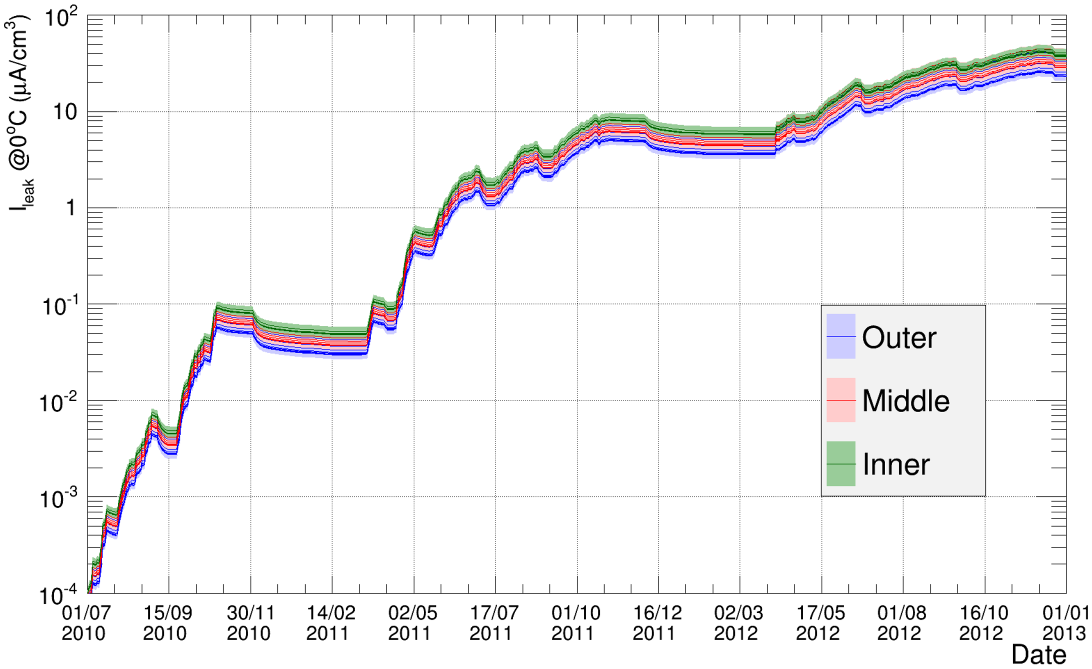

(b) Logarithmic scale

Figure 7.5: Predicted Leakage current evolution for all 22 regions of the end-caps categorised by their cylindrically radial position: outer, middle and inner.

Chapter 8

Observations of Leakage Current

8.1 SCT Power Supply

Each individual module of the SCT is powered by its own independent low and high voltage power supplies [1]. These operate at 50 V and 150 V, respectively. The low voltage supply is used as the standby power. The high voltage supply is the functional power supply of the sensor and, therefore, responsible for its depletion and charge carrier/signal collection. The SCT is served by a total of 4224 channels, which are divided in to 88 power supply crates. These are split equally between those for the barrel and end-cap region, 44 for each. A crate thus feeds 48 channels. The current registered for these channels may be extracted in order to determine the leakage current of each of the corresponding modules.

All 2112 barrel channels are hooked up to an equal number of detector modules. In end-cap assigned crates, 1976 individual channels correspond to operating modules. The remainder are unconnected, consistently registering a 0 nA current.

8.2 Raw Data

The raw data obtained for each channel consists of the absolute current measurements I_{read} in nA. Accompanying this reading is the corresponding date and time of the measurement in ms. Readings are for a given power supply crate and channel number. 2011 and 2012 data for all end-cap channels is processed. A majority subset of 2011 data for 1623 channels is processed for the barrel modules.

Example plots of leakage current versus time for a single module, in 2011 and 2012, are presented in figure 8.1. In both cases the data is for channel 0 of crate 9, which connects to an outer module of disc 3 in end-cap A.

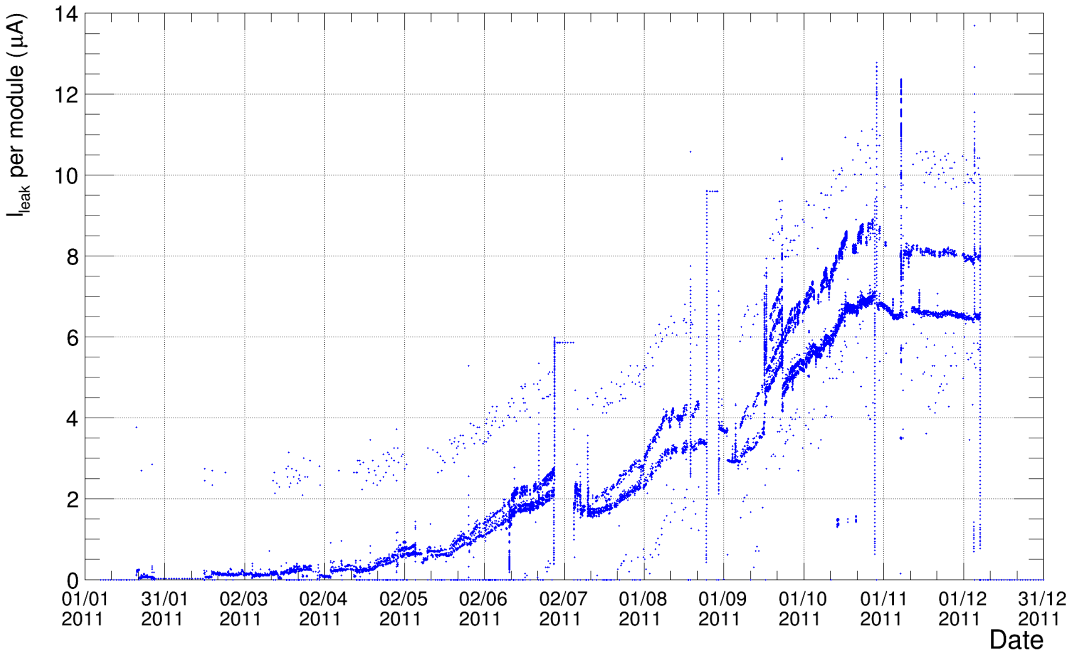

(a) 2011

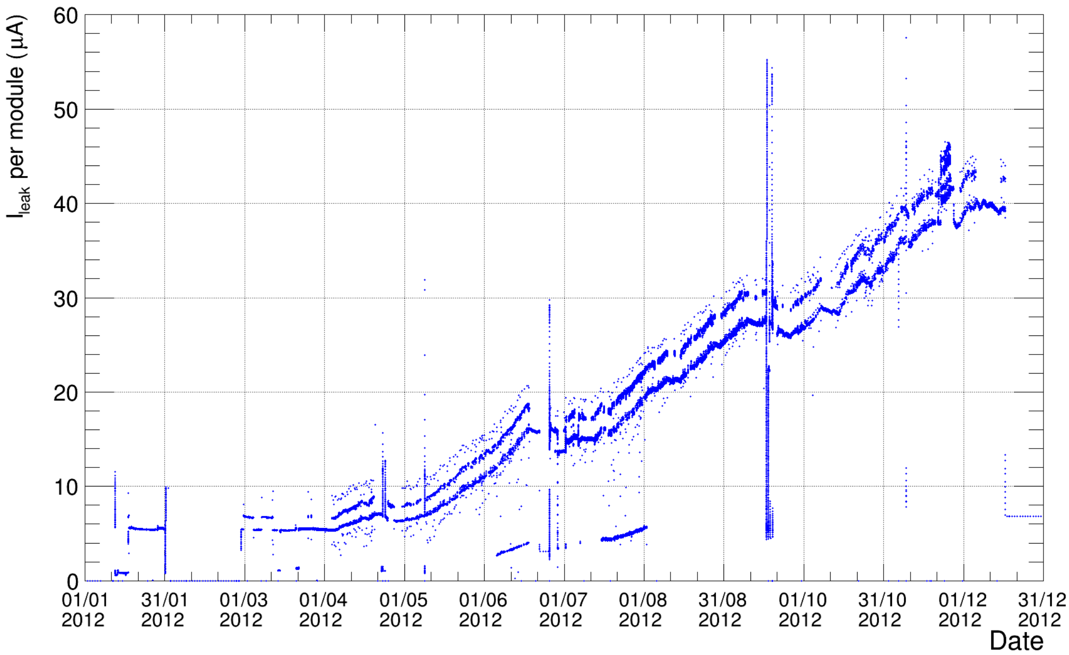

(b) 2012

Figure 8.1: Leakage current measurements for crate 9, channel 0. Note the signal due to high (top signal) and low (bottom signal) voltage current channels. Scattered points above and below these show ramp up and ramp down processes, respectively. The vertical spikes report current-voltage (IV) scans.

8.3 Extracting an Observation

A selection of I_{read} for the high voltage channel leakage current must be extracted for a given date. This is in order to compare it with the expected magnitude on the corresponding day. However, there is significant noise[1] in the readings (fig. 8.1).

Primarily this is due to the inconsequential standby voltage signal. As well as the scattered I_{read} due to ramp up and ramp down cycles, which are necessary when switching between the power supply channels. Also apparent are spikes due to current-voltage (IV) scans, which are used as part of the monitoring process [24]. To obtain the desired leakage current observation, it is necessary to exclude this data from the sample. Disconnected channels and those channels connected to non-responsive modules, which consistently register 0 nA throughout the year, are identified and disregarded.

Sample isolation is accomplished by successively limiting the observed time range and manually selecting a period during which the data is relatively noise free and dominated by high voltage operation (fig. 8.2). Once approved, a histogram is filled with the cropped data, and the maximum bin is extracted as the observed leakage current I_{data} on this date (Fig. 8.3).

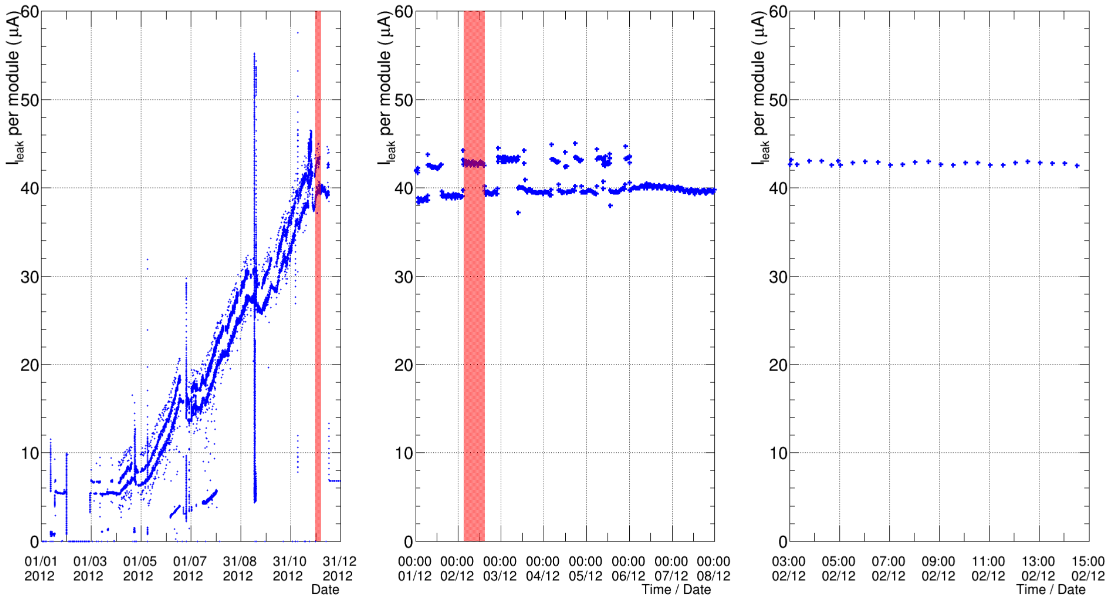

Figure 8.2: An example showing the successive cropping of leakage current data to between 3am and 3pm on 2nd December 2012. (Crate 9, Channel 0)

[1]'Noise' here may not be considered true noise, yet the term is used to distinguish all data that is not the required high voltage channel signal.

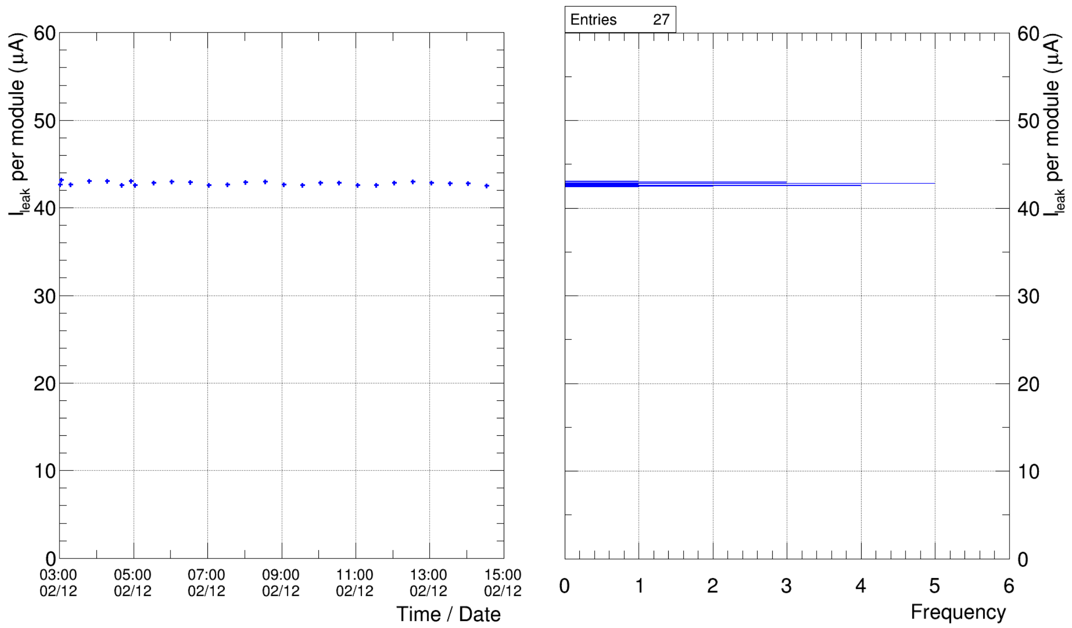

Figure 8.3: Frequency Histogram (Right) of data cropped between 3am and 3pm on 2nd December 2012 (Left). The maximum bin is extracted as the observed current for this date. (Crate 9, Channel 0)

The processes which cause the noise are universally applied to the SCT modules. This means that the manually selected range may then be used to filter the leakage current for all 4088 modules and obtain a full sample for all channels. A small number of modules, while responsive for the majority of the year, malfunction for short periods of time. Therefore, to filter these out, only extracted currents greater than 1 nA and less than 100 µA are accepted. This 'cleanses' the sample by removing anomalous extremes in current.

Each power supply channel and its affiliated current measurement is then mapped to the corresponding detector module coordinates, which signify its position in the SCT[2]. The result is a sample of the leakage current I_{data} for all modules of the Barrel and End-Cap on a particular date. Generally, these are extracted over time period between 6 and 24 hours. This sample is then normalised to the equivalent leakage current at 0 °C in the same manner as the normalised predictions:

$$I_{data} @ T_N = I_{data} \frac{1}{V} \left(\frac{T_N}{T_{Si}} \right)^2 exp \left[-\frac{E_g}{2k_B} \left(\frac{1}{T_N} - \frac{1}{T_{Si}} \right) \right] \tag{8.1}$$

Where V is the silicon area of each module species, given in table 5.3. T_N is the normalisation temperature chosen as 0 °C (273.15 K) and the silicon temperatures T_{Si} are those detailed in table 7.3.

[2]Mapping information was obtained from the database of the ATLAS SCT module search engine, prepared by J. E. Garcia [45]

8.4 Averaging Observations over Detector Regions

All the modules in a given region recieve the same fluence and are at the same temperature, theoretically (chapter 7). Hence, they should share the same leakage current evolution. Therefore, I_{data} @ 0 °C is averaged over angular position and layer, for end-cap and barrel samples, respectively. This gives: $\overline{I_{data}}$ @ 0 °C [3].

8.4.1 HPK and CiS

Before moving on, it is important to mention an issue with a subset of the modules which necessitates distinguishing them when taking the regional averages.

The modules of the SCT were custom built to the same specifications, however, the silicon sensors were constructed by two different manufacturers: Hamamatsu Photonics (HPK) and CiS. All barrel modules were constructed by the former, while 496 of 1976 of the end-cap modules were manufactured by CiS. Their distribution throughout the end-caps is reported in table 8.1.

End-Cap C										End-Cap A								
9	**8**	**7**	**6**	**5**	**4**	**3**	**2**	**1**	**Disc**	**1**	**2**	**3**	**4**	**5**	**6**	**7**	**8**	**9**
52	52	52	52	52	52	52	52	52	**Outer**	52	52	52	52	52	52	52	52	52
–	40_{40}	40	40	40_{40}	40_{40}	40_{40}	40_{10}	40	**Middle**	40	40_{10}	40_{40}	40_{40}	40_{40}	40	40	40_{40}	–
–	–	–	40_{38}	40_{40}	40	40	40	–	**Inner**	–	40	40	40	40_{38}	40_{40}	–	–	–

Table 8.1: Number of modules around each ring. Subscript red numbers show the number of CiS manufactured modules.

In 2012, anomalously high currents were noticed in a number of CiS modules. This resulted in ATLAS registering a high occupancy due to the noise [2]. This was found to occur during periods of high sustained luminosity (stable beams) of around $6.5 \times 10^{33}\,\mathrm{cm^{-2}s^{-1}}$. A plot showing the current differences between 9:30 and 14:30 for all end-cap modules on the 5th June 2012 is shown in figure 8.4.

It can be seen that the majority of 'normal' modules (predominantly HPK) show a moderate increase over this time, due to effects of bulk radiation damage. However, a large number of CiS modules show excessive increases over this short period. These then drop down to more reasonable current levels before the next period of stable irradiation. The reasons for these fluctuations are thought to be due to surface current effects (Section 4.7), caused by an accumulation of surface charge due to a small difference in design [46].

A plot of data cropped between the 1st September and 1st November 2011, for a middle module of disc 3 in end-cap A, is shown in figure 8.5. It demonstrates the characteristic rapid increases and decreases afflicting the affected CiS modules. This example is moderate compared to some modules which demonstrate fluctuations with a magnitude of over 8 µA, as shown in figure 8.4. The HM is designed to predict the evolution of bulk leakage current due to the effects of bulk radiation damage. Therefore, a distinction is made, when averaging by ring, between those modules with coordinates labelled CiS and those labelled as HPK.

[3] The overline notation $\overline{x}$ is used to distinguish mean values.

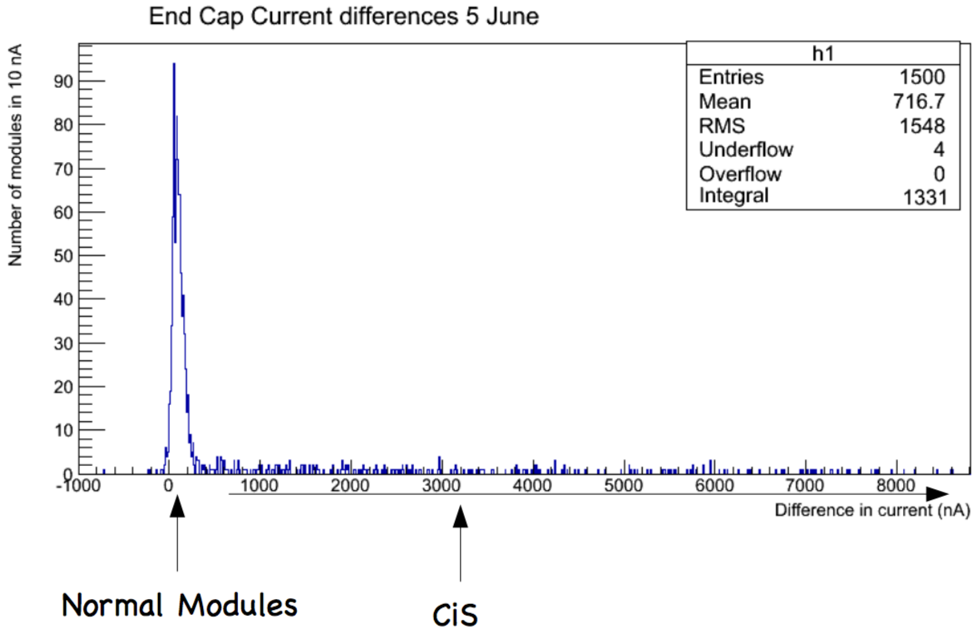

Figure 8.4: This plot shows the differences in current between 9:30 and 14:30 on 05/06/2012. The CiS modules show very large temporary fluctuations in current over short time periods [47]

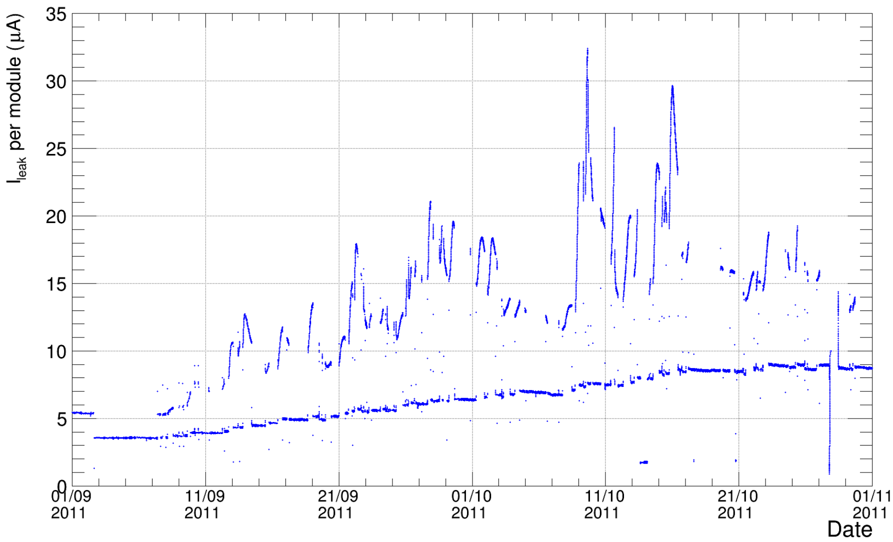

Figure 8.5: Leakage current measurements for a CiS middle module of disc 3 in end-cap 9 between 01/09/2011 and 01/11/2012. Note the short term rapid increases during successive stable beams, which drop off just as quickly. These surface events mask the evolution of bulk leakage current.

8.5 Averages of an End-Cap Sample

Table 8.2a shows the normalised leakage current I_{data} averaged over all modules in the ring, with no distinction between manufacturers. Tables 8.2b and 8.2c filter only HPK and CiS products, respectively. The CiS laden rings show significantly higher currents than the neighbouring HPK regions. Comparing table 8.2a with table 8.2b, it can be seen that in the regions incorporating both HPK and CiS modules, the averages are increased when not filtering out the later subset.

This effect would in fact be magnified greatly if it weren't for 'cleaning' during the extraction process (Section 8.3). Subsequently, in this analysis, HPK and CiS modules will always be distinguished between. The focus will be on the HPK modules, as they show significantly less interference from unpredictable surface currents.

Table 8.2b demonstrates that the regional averages for this sample show the characteristics expected from the fluence distribution in table 7.2. There is a general increase in leakage current at smaller r, closer to the the beam-line, and at higher $|z|$ values (Section 7.2). Also notable are the higher currents across all modules in the A side than in the C side. This is most likely due to a temperature difference between the two end-caps, which will be further discussed in the upcoming sections.

$\overline{\mathbf{I_{data}}}$ @ 0 °C [µA/cm^3]																		
End Cap C										**End Cap A**								
9	**8**	**7**	**6**	**5**	**4**	**3**	**2**	**1**	**Disc**	**1**	**2**	**3**	**4**	**5**	**6**	**7**	**8**	**9**
23.5	21.0	18.1	16.1	16.0	15.1	14.9	15.3	15.5	**Outer**	18.9	18.8	18.8	18.6	19.5	20.1	21.3	25.5	29.9
-	48.6	23.2	20.8	31.5	31.1	29.0	27.8	20.5	**Middle**	25.1	27.8	34.9	37.1	35.6	26.6	27.6	50.0	-
-	-	-	37.2	35.9	29.4	29.6	29.7	-	**Inner**	-	37.5	37.6	37.4	47.6	50.7	-	-	-

(a) All modules. Rings with 38/40+ CiS modules are highlighted in red. The brown highlight shows where a ring contains 10/40 CiS modules.

$\overline{\mathbf{I_{data}}}$ @ 0 °C [µA/cm^3]																		
End Cap C										**End Cap A**								
9	**8**	**7**	**6**	**5**	**4**	**3**	**2**	**1**	**Disc**	**1**	**2**	**3**	**4**	**5**	**6**	**7**	**8**	**9**
23.5	21.0	18.1	16.1	16.0	15.1	14.9	15.3	15.5	**Outer**	18.9	18.8	18.8	18.6	19.5	20.1	21.3	25.5	29.9
-	-	23.2	20.8	-	-	-	24.3	20.5	**Middle**	25.1	24.3	-	-	-	26.6	27.6	-	-
-	-	-	47.1	-	29.4	29.6	29.7	-	**Inner**	-	37.5	37.6	37.4	43.5	-	-	-	-

(b) HPK modules only

$\overline{\mathbf{I_{data}}}$ @ 0 °C [µA/cm^3]																		
End Cap C										**End Cap A**								
9	**8**	**7**	**6**	**5**	**4**	**3**	**2**	**1**	**Disc**	**1**	**2**	**3**	**4**	**5**	**6**	**7**	**8**	**9**
-	-	-	-	-	-	-	-	-	**Outer**	-	-	-	-	-	-	-	-	-
-	48.6	-	-	31.5	31.1	29.0	38.4	-	**Middle**	-	38.4	34.9	37.1	35.6	-	-	50.0	-
-	-	-	36.7	35.9	-	-	-	-	**Inner**	-	-	-	-	47.8	50.7	-	-	-

(c) CiS modules only

Table 8.2: End-Cap normalised leakage currents averaged over each ring for a sample extracted between 3am and 3pm on the 2nd December 2012.

Chapter 9

Comparing Expected and Observed Leakage Current

In the previous chapter, samples I_{data} were made of observations extracted for a given range of time, on a certain date. As a consequence of detector symmetry these were then averaged over each ring to give $\overline{I_{data}}$. Now, for each detector region, a HM predicted normalised leakage current I_{HM} is selected for the corresponding day. The ratio of observed over expected leakage current is then taken for each region.

$$R_{leak} = \frac{\overline{I_{data}}}{I_{HM}} \tag{9.1}$$

As before HPK and CiS are treated with distinction. The results for a single sample, extracted on the 2nd December 2012, are shown in tables 9.1a and 9.1b. Note that this sample is made example of throughout this and the previous section in order to show the path from raw data to the final regional comparisons.

Table 9.1a shows that there is a general agreement in ratio for modules of the same radial distance. In other words, all the outer modules of each side show comparable ratios. For the HPK modules, the inner modules of disc 6 and 5 of end-cap C and A, respectively, are higher. There are only 2 HPK modules in this ring, and these, therefore, have poor statistical significance. They are excluded from subsequent averages. Clearly, the ratios of observed to expected leakage current are higher in end-cap A. Again, this will be discussed shortly.

$R_{leak} = \overline{I_{data}} / I_{HM}$																		
End Cap C										**End Cap A**								
9	**8**	**7**	**6**	**5**	**4**	**3**	**2**	**1**	**Disc**	**1**	**2**	**3**	**4**	**5**	**6**	**7**	**8**	**9**
0.57	0.58	0.58	0.57	0.61	0.59	0.59	0.61	0.61	**Outer**	0.75	0.74	0.75	0.72	0.74	0.72	0.69	0.70	0.72
-	-	0.61	0.60	-	-	-	0.78	0.65	**Middle**	0.80	0.78	-	-	-	0.77	0.73	-	-
-	-	-	1.07	-	0.71	0.74	0.73	-	**Inner**	-	0.92	0.93	0.90	1.03	-	-	-	-

(a) HPK modules

$R_{leak} = \overline{I_{data}} / I_{HM}$																		
End Cap C										**End Cap A**								
9	**8**	**7**	**6**	**5**	**4**	**3**	**2**	**1**	**Disc**	**1**	**2**	**3**	**4**	**5**	**6**	**7**	**8**	**9**
-	-	-	-	-	-	-	-	-	**Outer**	-	-	-	-	-	-	-	-	-
-	1.10	-	-	0.97	0.96	0.93	1.23	-	**Middle**	-	1.23	1.12	1.14	1.09	-	-	1.13	-
-	-	-	0.83	0.85	-	-	-	-	**Inner**	-	-	-	-	1.13	1.15	-	-	-

(b) CiS modules

Table 9.1: End-Cap ratio of observed to predicted leakage current, by region.

9.1 Wider Averaging

In order to evaluate the evolution of these ratios over time it is necessary to make more generalised averages $\overline{R_{leak}}$.

$$\overline{R_{leak}} = \overline{\left(\frac{\overline{I_{data}}}{I_{HM}}\right)} \tag{9.2}$$

To this effect, the mean is taken for all modules of a particular manufacturer. All HPK modules from every region of the detector are averaged over, and, likewise for CiS. Particular focus is given to the HPK modules, as these are more representative of the bulk radiation damage. Thus, the mean of these is taken at each radial distance, over every disc. For example:

$$\overline{R_{leak}} = \overline{\left(\frac{\overline{I_{data}}}{I_{HM}}\right)}\Bigg|_{all\ CiS} \quad ; \quad \overline{R_{leak}} = \overline{\left(\frac{\overline{I_{data}}}{I_{HM}}\right)}\Bigg|_{outer\ HPK} \tag{9.3}$$

Throughout this process the error due to temperature uncertainty has been accounted for. At lower assumed silicon temperature T_{Si}, I_{leak} decreases exponentially. Therefore, the error in I_{HM} is asymmetric. Note that the denominator of R_{leak} is I_{HM}. Thus, increases in theoretical leakage current result in smaller ratios. It follows that the upper error in R_{leak} corresponds to a lower error band in I_{HM}, This greater in magnitude than the lower error due to the asymmetry in uncertainty.

In the Harper model, temperature and fluence are independent variables, therefore, the relative errors due to uncertainty in luminosity and temperature are added in quadrature. This also means that the relative uncertainty in I_{HM} for a given day is uniform for all regions of the end-caps, as these are assumed to be at the same temperature. Barrel 6, however, has a different relative uncertainty to the other barrels. This due to the known difference in temperature. Note that, for this section, the regions of neutral fluence encompass each barrel layer, so no further averaging of R_{leak} is necessary.

An example of the wider averages for an end-cap sample is given in table 9.2.

		$\overline{R_{leak}} = \overline{\overline{I_{data}} / I_{HM}}$					
		End Cap C			End Cap A		
Manufacturer	**Modules**	$-$	Mean	$+$	$-$	Mean	$+$
HPK	All	0.059	0.62	0.066	0.073	0.77	0.081
HPK	Outer	0.056	0.59	0.062	0.069	0.73	0.076
HPK	Middle	0.073	0.62	0.081	0.073	0.77	0.081
HPK	Inner	0.069	0.73	0.076	0.087	0.92	0.097
CiS	All	0.090	0.96	0.100	0.108	1.14	0.120

Table 9.2: Broad regional averages for the 2nd December end-cap sample. Featured are the lower (-) and upper (+) error due to uncertainty in the HM input.

9.2 Barrel Results

Nine data samples were extracted for the barrel modules at multiple times in 2011. The purpose of this was to cross-check these results with those of a contemporary study performed by T. Kondo [3]. Plots of I_{data} against I_{HM}, with both linear and logarithmic scales, are shown in figures 9.1a and 9.1b, respectively. The ratio of these measurements R_{leak} is then taken and shown in figure 9.2.

The results for the barrel modules show that the measurements follow the shape of the expected evolution. The I_{data} distribution increases with integrated luminosity and decreases during periods of zero or low luminosity, due to beneficial annealing. There is a systematic deviation between I_{data} and I_{HM} throughout the year. This is demonstrated in table 9.3. All barrels have a mean ratio, over all samples, of around 0.9, with standard deviations of about 0.03.

These results are consistent with those findings presented in the previous study of the barrel modules (Section 1.2). This supports the validity of the analytical method for use with the end-cap modules. The larger error bands in the plot from the parallel study come from the uncertainty in the Harper model amplitudes and time constants (tab. 6.1). These parameters were assumed to have independent errors and significantly increase the final uncertainty in the predictions. These factors were not addressed in this analysis.

Modules	$\overline{\overline{R_{leak}}\vert_{time}}$	σ
B6	0.89	0.025
B5	0.92	0.031
B4	0.91	0.032
B3	0.91	0.032

Table 9.3: The time averaged mean and standard deviation of barrel module R_{leak} over all samples in 2011 and 2012.

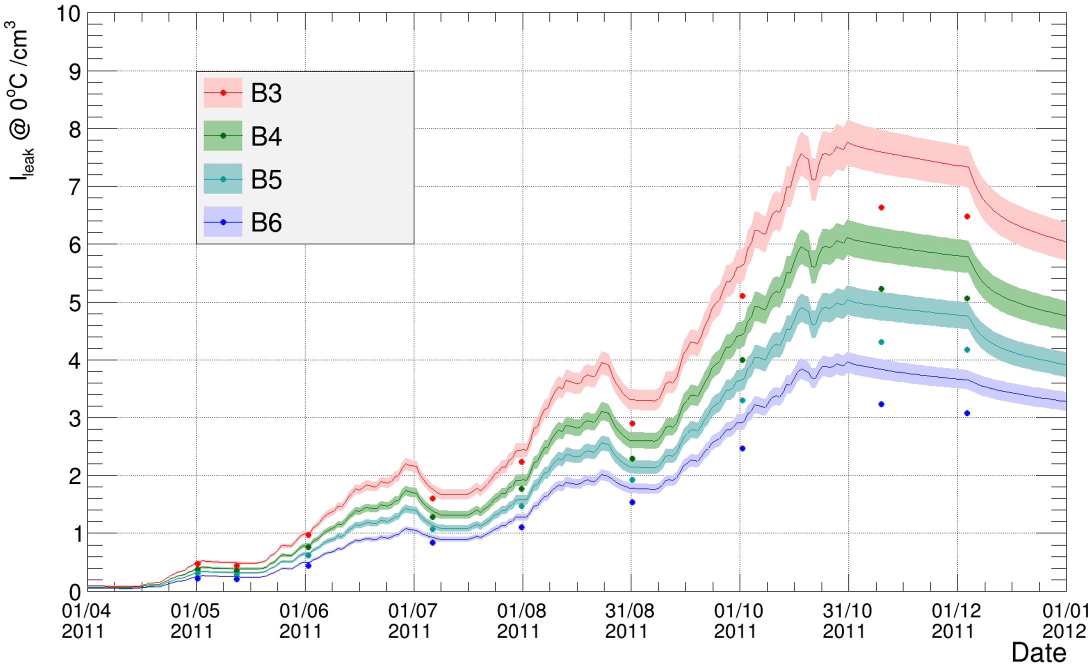

(a) Linear scale

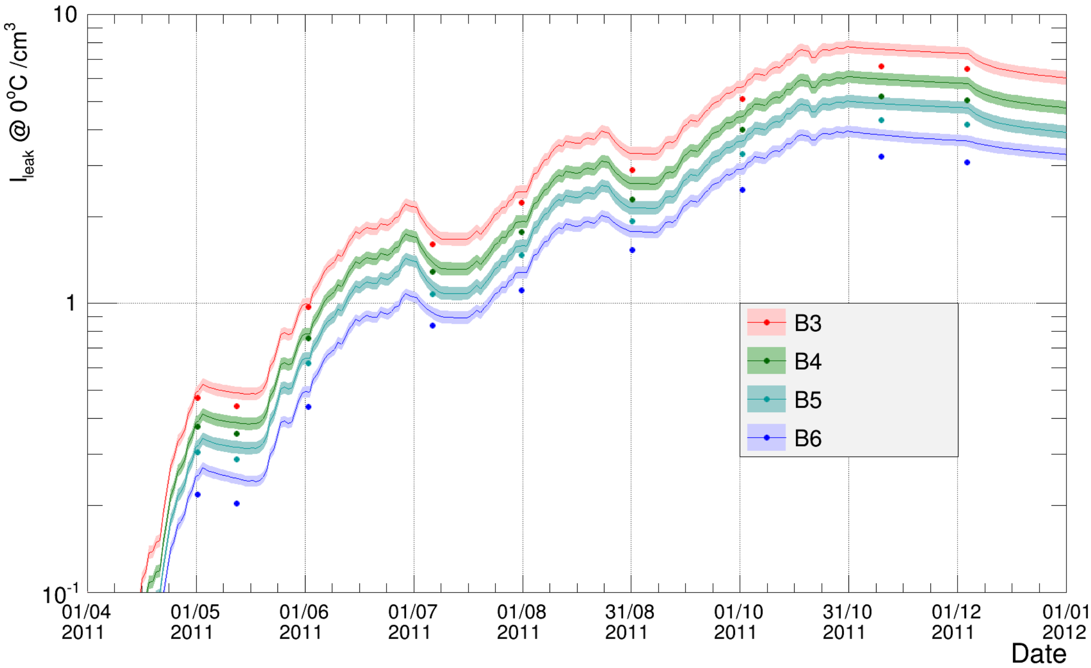

(b) Logarithmic Scale

Figure 9.1: Observed Leakage current I_{data} (points) plotted against the predicted evolution I_{HM} (lines) for each layer of the Barrel with I_{HM} uncertainty reported by coloured bands.

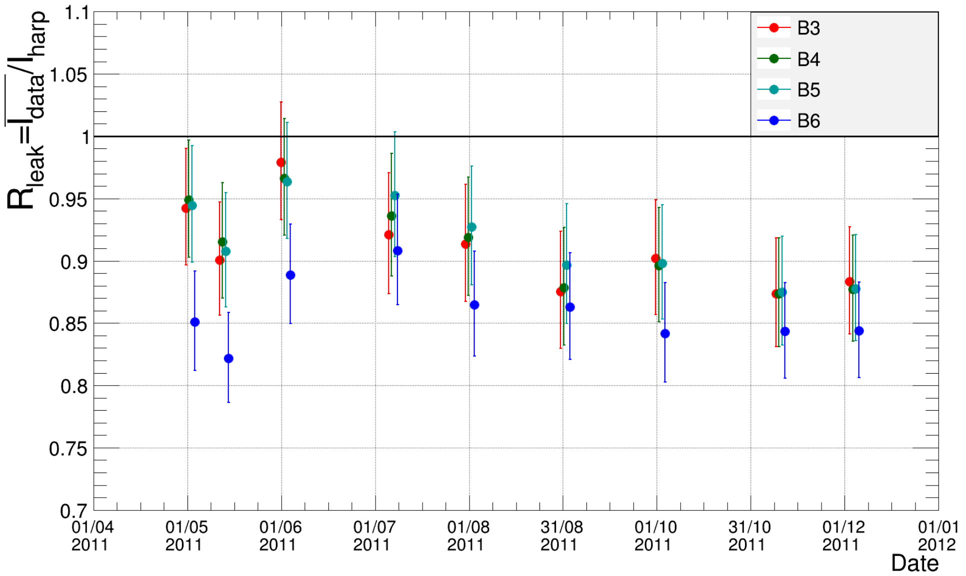

Figure 9.2: Ratio of Observed to Predicted Leakage Current for each layer of the Barrel. Barrel layers are offset by a few days from B4 for clearer presentation.

9.3 End-Cap Results

Twenty end-cap samples were extracted and compared with predictions at multiple times in 2011 and 2012. Broader regional averages were then made (Section 9.1). The results for all modules, distinguishing between manufacturers, are displayed in figures 9.3a and 9.3b, respectively, for end-cap C and A. Breakdown plots for the inner, middle and outer HPK modules of end-cap C and A are shown in figures 9.4a and 9.4b, respectively.

The average ratio $\overline{R_{leak}}$ of all HPK modules in both end-caps shows a seemingly level distribution across time. This shows that the observed leakage current follows the shape of the theoretical evolution from the start of 2011 to end of 2012. Therefore, regardless of magnitude, it suggests any disparity is uniform over time, neither increasing nor decreasing.

Another significant visual difference between figures 9.3b and 9.3a is the persistently higher distribution of ratios for end-cap A than end-cap C. From table 9.4 the difference in the mean, between A and C, of HPK modules throughout the analysed period is approximately 1.5. This is significantly greater than the standard deviation of either. The reason for this asymmetry is likely due to a difference in temperature between A and C.

Direct measurements of the liquid coolant suggest side A is approximately 2 °C higher than side C. However, while relative difference are suggested, due to the limits in attaining absolute silicon temperatures for the end-caps, an accurate temperature profile cannot, presently, be established (section 7.4)[1].

[1]The absolute temperatures of the sensors in end-cap modules are a subject of ongoing research, therefore, there have been no published analyses at the present time.

The $\overline{R_{leak}}$ distributions of radially separated subsets are approximately parallel to those for all HPK in A and C. It follows that I_{data} for the modules in these individual regions are maintaining a consistent deviation from I_{HM} over time. The temperature difference between A and C is again notable by the generally higher magnitudes for all $\overline{R_{leak}}$ on the A-side.

The differences in the distribution of $\overline{R_{leak}}$ for outer, middle and inner rings show a clear pattern across the 2 years. These differences are highlighted by the temporal averages in table 9.4. Inner modules on both sides have the highest average ratio, followed by those in the middle ring. The outer module ratios are lowest. Unconfirmed temperature differences between different radii may explain these findings. This is to say that the temperature distribution in the end-caps may be a function of the cylindrical radius: $T_{Si}(r)$.

In all cases I_{data} is shown to be consistently below I_{HM} for HPK modules. Some of this discrepancy may be attributed to the disregard for uncertainty in the Harper model constants. However, the findings clearly favour the consistency of measured evolution with the theoretical advancement, given the known parameters.

The CiS modules show a far less consistent pattern. $\overline{R_{leak}}$ fluctuates greatly over time. These fluctuations are attributable to the susceptibility of these modules to surface current effects, which interfere with bulk current observation. This phenomenon was noticed and established only in 2012, two years after the 2010 study which found the high discrepancy for inner end-cap modules. Speculatively, this factor may have been unaccounted for in the 2010 study, leading to the perceived high discrepancy between bulk current prediction and measurements. Figure 8.5 shows that the characteristic rapid increase in leakage current, during stable beams, occurred at least as early as 2011.

	End-Cap C		End-Cap A	
Modules	$\overline{\overline{R_{leak}}\vert_{time}}$	σ	$\overline{\overline{R_{leak}}\vert_{time}}$	σ
All	0.61	0.038	0.76	0.031
Outer	0.59	0.040	0.72	0.032
Middle	0.60	0.029	0.75	0.031
Inner	0.69	0.050	0.87	0.038

Table 9.4: The time averaged mean and standard deviation for End-Cap HPK module R_{leak} over all samples in 2011 and 2012.

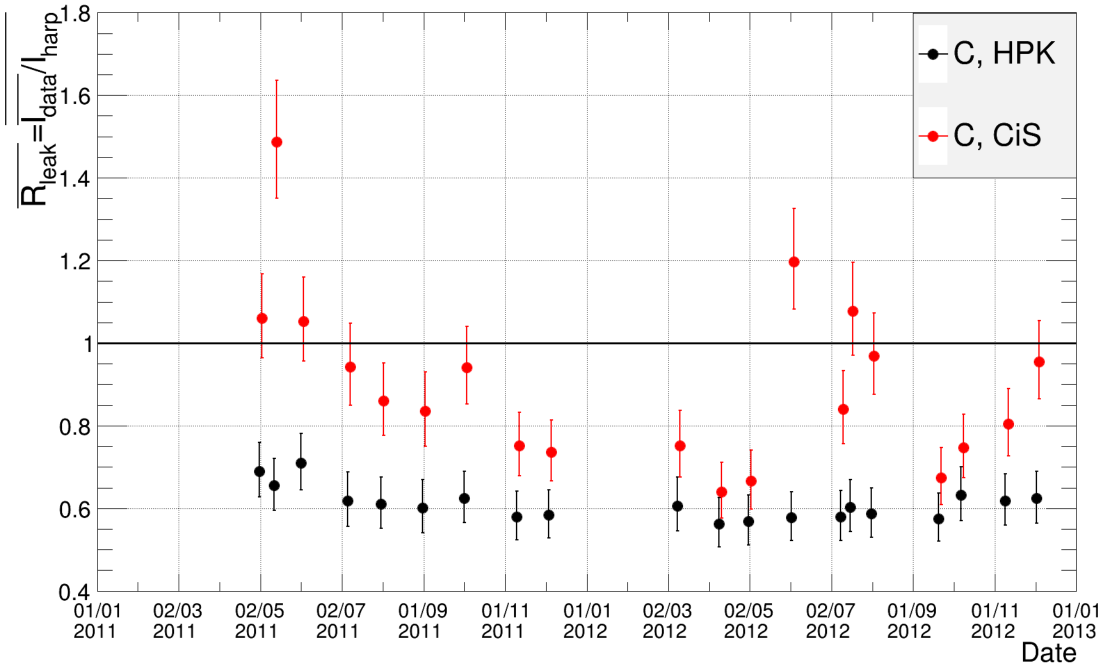

(a) End-Cap C

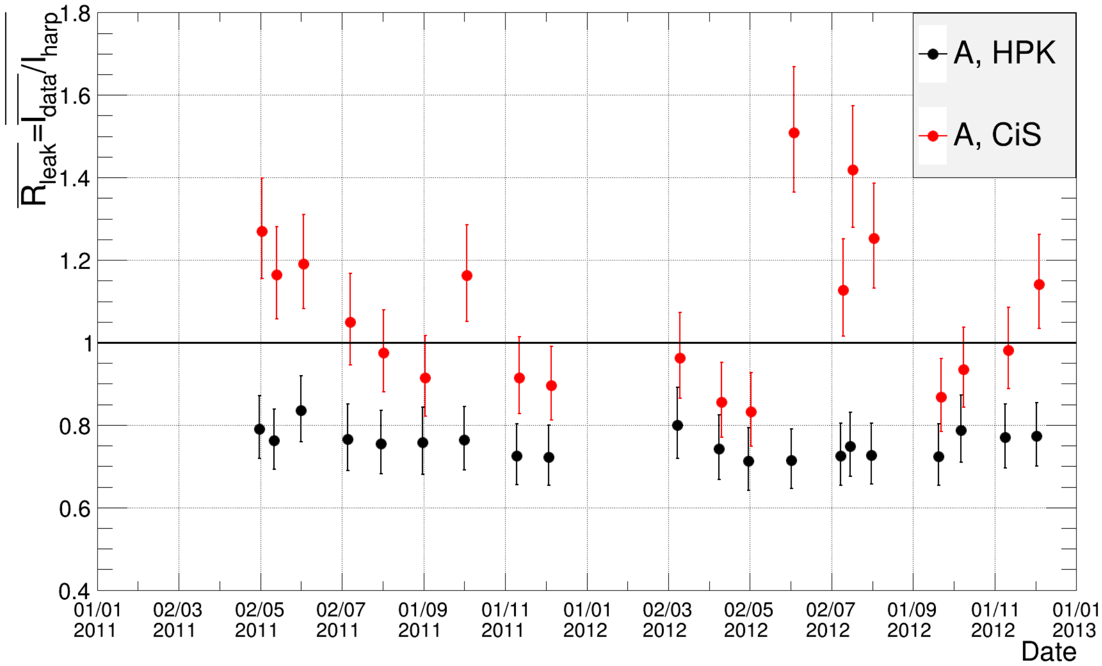

(b) End-Cap A

Figure 9.3: $\overline{R_{leak}}$ for HPK and CiS, averaged all rings. HPK module points are set on the day of the sample, with CiS modules displayed two days to the right, for increased visibility.

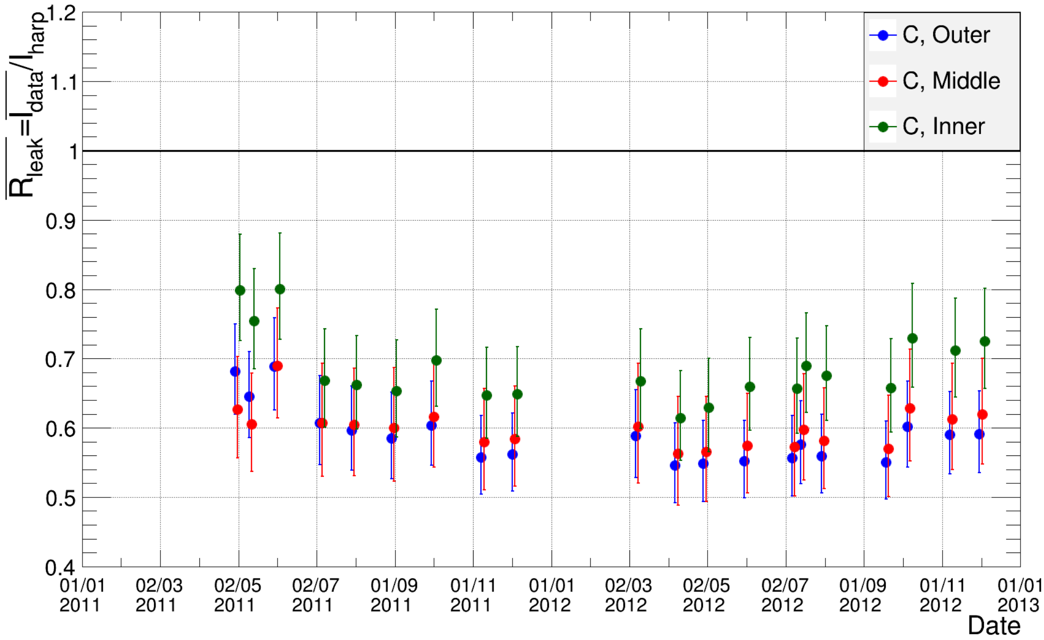

(a) End-Cap C

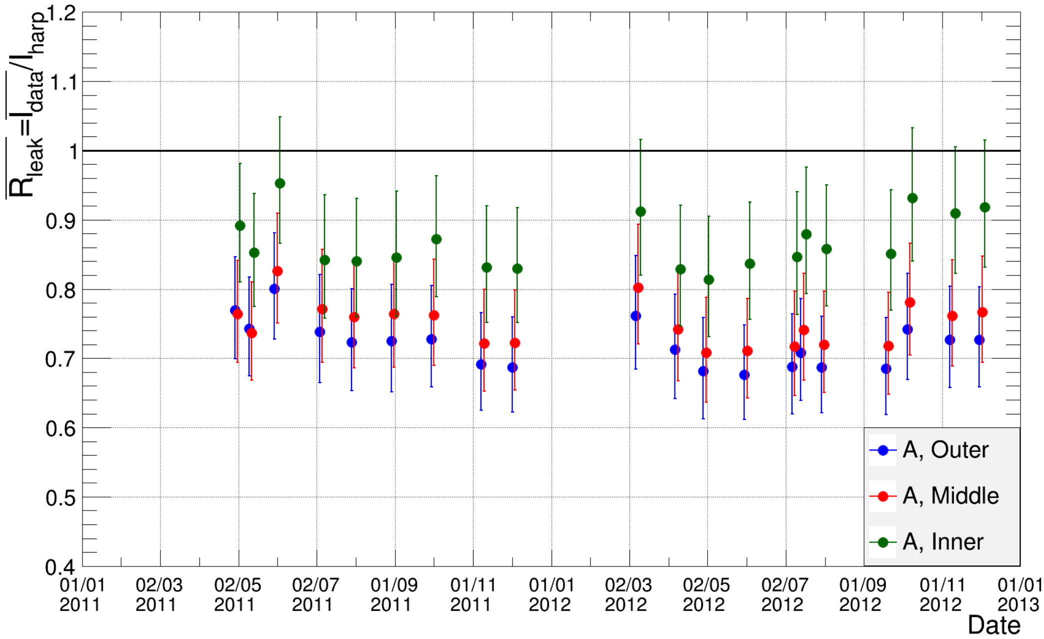

(b) End-Cap A

Figure 9.4: $\overline{R_{leak}}$ for outer, middle and inner HPK modules, averaged over all discs. Middle module points are set on the day of the sample, with inner and outer modules displayed two days to the right and left, respectively, for increased visibility.

Chapter 10

Conclusions

An analysis of the leakage current in the end-cap modules of the ATLAS SCT has been performed for 2011 and 2012 data. Samples of the measured leakage current I_{data} were extracted and compared with the Harper model predictions. This was done by taking the ratio $R_{leak} = \overline{I_{data}} / I_{HM}$.

On average, HPK manufactured modules in both end-cap A and C show a seemingly level R_{leak} distribution over time. This is reflected individually for inner, middle and outer modules. This suggests that the leakage current is following the expected evolution. R_{leak} for end-cap A is systematically higher than in end-cap C, with the difference in mean for all HPK modules at around 1.5. This is likely due to a temperature difference between the two sides. The outer, middle and inner ratios also show persistent differences across the 2 years: $R_{inner} > R_{middle} > R_{outer}$. This disparity may result from a radial temperature distribution in the end-caps.

In all cases, for HPK modules, I_{data} is shown to be consistently below I_{HM}. This difference may be reduced by accounting for uncertainty in the Harper model parameters. However, the clear suggestion is that the measured evolution in leakage current of the ATLAS SCT end-cap modules is systematically lower than expected from the theoretical evolution. Assuming the continuation of this trend, the current will remain within functional bounds for the proposed life of the ATLAS detector. This suggests that the radiation damage to the silicon bulk is advancing at a foreseen and acceptable rate.

Significantly higher I_{data} was observed in CiS modules, an observation attributable to surface currents. Speculatively, the surface interference across these modules may have been responsible for the high R_{leak} at low radii in the 2010 study of the end-caps. An analysis of the barrel modules for 2011 data also confirms that I_{data} is evolving as expected. The equivalence between these results and those of a parallel study provides support for the validity of the end-cap analysis.

Bibliography

[1] P. Phillips. "ATLAS SCT Power Supply System". In: *Proceedings of the Topical Workshop on Electronics for Particle Physics* (2007), pp. 365–368. URL: http://cdsweb.cern.ch/record/1091485/.

[2] S. McMahon, D Robinson, P Dervan, et al. "ATLAS Semiconductor Tracker (Strips)". In: *Presented at the 19th RD50 Workshop* (Nov. 2011). URL: https://indico.cern.ch/getFile.py/access?contribId=69\&sessionId=4\&resId=0\&materialId=slides\&confId=148833.

[3] T. Kondo. "ATLAS Silicon Bulk Radiation Damage Studies". In: *Presented at the Second Inter-Experiment Workshop on Radiation Damage in Silicon Detectors* (Mar. 2012).

[4] A. Jeff, A. Boccardi, E. Bravin, et al. "First results of the LHC longitudinal density monitor". In: *Nuclear Instruments and Methods in Physics Research Section A: Accelerators, Spectrometers, Detectors and Associated Equipment* 659.1 (Dec. 2011), pp. 549–556. ISSN: 01689002. DOI: 10.1016/j.nima.2011.08.055. URL: http://linkinghub.elsevier.com/retrieve/pii/S0168900211017165.

[5] L. Evans and P Bryant. "LHC machine". In: *Journal of Instrumentation* (2008). URL: http://iopscience.iop.org/1748-0221/3/08/S08001.

[6] B. M. Demirköz. "Construction and Performance of the ATLAS SCT Barrels and Cosmic Tests". PhD thesis. Balliol College, University of Oxford, 2007, p. 227.

[7] D. H. Perkins. *Introduction to High Energy Physics*. 4th Edition. Cambridge University Press, 2000.

[8] F. Halzen and A. D. Martin. *Quarks and Leptons: an introductory course in modern particle physics*. Wiley, 1987.

[9] The Atlas Collaboration. "Combined measurements of the mass and signal strength of the Higgs-like boson with the ATLAS detector using up to 25 fb-1 of proton-proton collision". In: *ATLAS NOTE* (2013), pp. 1–14.

[10] The Atlas Collaboration. "Study of the spin of the new boson with up to 25 fb1 of ATLAS dataote". In: *ATLAS Note* (2013), pp. 1–15.

[11] S Moretti, S Munir, and P Poulose. "The 125 GeV Higgs Boson signal within the Complex NMSSM". In: *arXiv preprint arXiv:1305.0166* April (2013). arXiv:arXiv:1305.0166v1. URL: http://arxiv.org/abs/1305.0166.

[12] G. Aad, E. Abat, J. Abdallah, et al. "The ATLAS experiment at the CERN large hadron collider". In: *Journal of . . .* (2008). URL: http://iopscience.iop.org/1748-0221/3/08/S08003.

[13] J. Pequenao. "Computer generated image of the whole ATLAS detector". 2008. URL: http://cds.cern.ch/record/%201095924.

[14] A. Abdesselam, P. P. Allport, B. Anderson, et al. "Engineering for the ATLAS SemiConductor Tracker (SCT) end-cap". In: *Journal of Instrumentation* 3 (2008). URL: http://iopscience.iop.org/1748-0221/3/05/P05002.

[15] B. Dolgoshein. "Transition Radiation Detectors". In: *Nuclear Instruments and Methods in Physics Research Section A: Accelerators, Spectrometers, Detectors and Associated Equipment* 326.3 (Mar. 1993), pp. 434–469. ISSN: 01689002. DOI: 10.1016/0168-9002(93)90846-A. URL: http://linkinghub.elsevier.com/retrieve/pii/016890029390846A.

[16] S. J. Blundell and K. M. Blundell. *Concepts in Thermal Physics*. 2nd Edition. Oxford University Press, 2010.

[17] S. M. Sze. *Physics of Semiconductor Devices*. 2nd Edition. John Wiley & Sons, Inc., 1981.

[18] A. R. Barron. "Band Gap Measurement (Image)". 2012. URL: http://cnx.org/content/m43554/latest/.

[19] H. P. Myers. *Introductory Solid State Physics*. 2nd Edition. Taylor and Francis Ltd. 1 Gunpowder Square, London, UK.: Taylor and Francis, 1990.

[20] TheNoise. "p-n Junction in Equilibrium (Image)". 2007. URL: http://en.wikipedia.org/wiki/File:Pn-junction-equilibrium.png.

[21] M. Moll. "Radiation Damage in Silicon Detectors". PhD thesis. Hamburg: University of Hamburg, 1999, p. 251. URL: http://mmoll.web.cern.ch/mmoll/thesis/pdf/moll-thesis.pdf.

[22] K. Roy. "Leakage current mechanisms and leakage reduction techniques in deep-submicrometer CMOS circuits". In: *Proceedings of the IEEE* 91.2 (2003), pp. 305 –327. URL: http://ieeexplore.ieee.org/xpls/abs_all.jsp?arnumber=1182065.

[23] A. Clark, M. Donega, M. DOnofrio, et al. "Design and test of a prototype silicon detector module for ATLAS Semiconductor Tracker endcaps". In: *Nuclear Instruments and Methods in Physics Research Section A: Accelerators, Spectrometers, Detectors and Associated Equipment* 538.1-3 (Feb. 2005), pp. 265–280. ISSN: 01689002. DOI: 10.1016/j.nima.2004.09.001. URL: http://linkinghub.elsevier.com/retrieve/pii/S0168900204020297.

[24] A. Abdesselam, P. J. Adkin, J. Alonso, et al. *ATLAS SCT Endcap Module Production*. Tech. rep. ATLAS SCT Collaboration, 2006, pp. 51–53. URL: http://cdsweb.cern.ch/record/973395/.

[25] H. Spieler. *Semiconductor Detector Systems*. 2nd Edition. Oxford University Press, 2006.

[26] A. Strandlie and R Frühwirth. "Track and vertex reconstruction: From classical to adaptive methods". In: *Reviews of Modern Physics* (2010). URL: http://rmp.aps.org/abstract/RMP/v82/i2/p1419_1.

[27] E Fretwurst, G Lindstrom, I Pintilie, et al. "Radiation Damage in Silicon Detectors Caused by Hadronic and Electromagnetic Irradiation". In: *arXiv preprint physics/0211118* December (2002). arXiv:0211118 [physics]. URL: http://arxiv.org/abs/physics/0211118.

[28] R Wunstorf. "Radiation Hardness of Silicon Detectors: Current Status". In: *IEEE Transactions on Nuclear Science* 44.3 (1997), pp. 806–814. URL: http://ieeexplore.ieee.org/xpls/abs_all.jsp?arnumber=603757.

[29] R. Harper. "Radiation Damage Studies of Silicon Detectors and Searching for an Intermediate Mass Higgs Boson at ATLAS". PhD thesis. Sheffield: University of Sheffield, 2001.

[30] A Chilingarov. *Generation Current Temperature Scaling*. Tech. rep. Lancaster: Lancaster University, 2011. URL: http://scholar.google.com/scholar?hl=en\&btnG=Search\&q=intitle:Generation+current+temperature+scaling\#8.

[31] J. Roberts. "The ATLAS Semiconductor Tracker". Masters Thesis. Southampton: University of Southampton, 2012, p. 88.

[32] T. Kondo. *SCT Leakage Current*. 2012. URL: https://twiki.cern.ch/twiki/bin/viewauth/Atlas/SctLeakageCurrent#Presentations_reverse_chronologi.

[33] P. S. M. Ian Dawson. *Benchmarking at the LHC*. 2012. URL: https://twiki.cern.ch/twiki/bin/viewauth/Atlas/BenchmarkingAtTheLHC.

[34] T Sjöstrand, S Mrenna, and P Skands. "A Brief Introduction to PYTHIA 8.1". In: *Computer Physics Communications* October (2008), pp. 1–27. arXiv:arXiv:0710.3820v1. URL: http://www.sciencedirect.com/science/article/pii/S0010465508000441.

[35] A Fasso, A Ferrari, and S Roesler. "The Physics Models of FLUKA: Status and Recent Development". In: *arXiv preprint hep-ph/...* 1232 (2003). arXiv:0306267v1 [arXiv:hep-ph]. URL: http://arxiv.org/abs/hep-ph/0306267.

[36] I. Dawson, I. Dervan, I. Mandic, et al. "Fluence and dose measurements in the ATLAS inner detector and comparison with simulation". In: 09.1020 (2011).

[37] D. J. Griffiths. *Introduction to Electrodynamics*. Ed. by K. Dellas. 3rd Edition. Prentice Hall Inc., 1999.

[38] J. Hubbell. "Electronpositron pair production by photons: A historical overview". In: *Radiation Physics and Chemistry* 75.6 (June 2006), pp. 614–623. ISSN: 0969806X. DOI: 10.1016/j.radphyschem.2005.10.008. URL: http://linkinghub.elsevier.com/retrieve/pii/S0969806X0500263X.

[39] S. Eidelman, H. Bichsel, D. E. Groom, et al. "Passage of Particles Through Matter". In: *Physics Letters* 1.B592 (2006). URL: http://pdg.lbl.gov/2005/reviews/passagerpp.pdf.

[40] W. Herr and B. Muratori. "Concept of luminosity". In: *Proceedings CAS2003, CERN-...* 2.3 (2006). URL: http://lhc-beam-beam.web.cern.ch/lhc-beam-beam/papers/lum.ps.

[41] The ATLAS Collaboration. "Luminosity determination in pp collisions at\ sqrt {s}= 7 TeV using the ATLAS detector at the LHC". In: *The European Physical ...* (2011), pp. 0–60. arXiv:arXiv:1101.2185v1. URL: http://link.springer.com/article/10.1140/epjc/s10052-011-1630-5.

[42] G. Unal. *ATLAS Public Luminosity Results*. 2013. URL: https://twiki.cern.ch/twiki/bin/view/AtlasPublic/LuminosityPublicResults.

[43] T. Kondo. "End-Cap Leakage Current Issues". In: *Presented at the SCT Weekly* (Apr. 2013).

[44] D. Attree, B. Anderson, E. C. Anderssen, et al. "The Evaporative Cooling System for the ATLAS Inner Detector". In: *Journal of Instrumentation* 3.7 (2008), pp. 1–36. DOI: 10.1088/1748-0221/3/07/P07003. URL: http://iopscience.iop.org/1748-0221/3/07/P07003.

[45] J. E. Garcia. *ATLAS SCT Coordinate database*. 2011. URL: https://pc-sct-www01.cern.ch/ModInfo/Coordinates/Coordinates.txt.

[46] S. D'Auria. "The ATLAS Semiconductor Tracker Operation and Performance". In: *2012 IEEE Nuclear Science Symposium and Medical Imaging Conference*. Ed. by The Atlas Collaboration. Anaheim, California, USA: IEEE, 2012, pp. 1–3. URL: https://cds.cern.ch/record/1494558/files/ATL-INDET-PROC-2012-027.pdf.

[47] S. D'Auria and N. Barlow. "CiS Sensor Currents and Onset of the Feature". In: *Presented to the SCT Collaboration* (June 2012).